

On the use of circulant matrices for the stability analysis of recent weakly compressible SPH methods

G. Chaussonnet^a, R. Koch^a, H.-J. Bauer^a

^aKarlsruher Institut für Technologie - Institut für Thermische Strömungsmaschinen, Karlsruhe, Germany

Abstract

In this study, a linear stability analysis is performed for different Weakly Compressible Smooth Particle Hydrodynamics (WCSPH) methods on a 1D periodic domain describing an incompressible base flow. The perturbation equation can be vectorized and written as an ordinary differential equation where the coefficients are circulant matrices. The diagonalization of the system is equivalent to apply a spatial discrete Fourier transform. This leads to stability conditions expressed by the discrete Fourier transform of the first and second derivatives of the kernel. Although spurious modes are highlighted, no tensile nor pairing instabilities are found in the present study, suggesting that the perturbations of the stresses are always damped if the base flow is incompressible. The perturbations equation is solved in the Laplace domain, allowing to derive an analytical solution of the transient state. Also, it is demonstrated analytically that a positive background pressure combined with the uncorrected gradient operator leads to a reordering of the particle lattice. It is also shown that above a critical value, the background pressure leads to instabilities. Finally, the dispersion curves for inviscid and viscous flows are plotted for different WCSPH methods and compared to the continuum solution. It is observed that a background pressure equal to ρc^2 gives the best fidelity to predict the propagation of a sound wave. When viscosity effects are taken into account, the damping of pressure fluctuations show the best agreement with the continuum for $p_{back} \sim \rho c^2/2$.

Keywords: weakly compressible SPH, dispersion relation, circulant matrix, background pressure, δ -SPH, Transport Velocity SPH

1. Introduction

The Smoothed Particles Hydrodynamics (SPH) method was initiated by Gingold and Monaghan [1] and Lucy [2] to study star formation. It is a second-order [3] Lagrangian method resolving and storing physical quantities (mass, momentum, energy) on spatial discretization points, so-called particles, which move with the local fluid velocity. The interaction between several particles is taken into account with a weighting function which promotes the influence of closer particles. This function is called the *kernel*. SPH was later extended to fluid mechanics [4], based on a weakly compressible approach that is commonly used nowadays. In the context of multiphase flow simulation, the main advantage of SPH over traditional grid-based methods is the intrinsic capturing of the phase interface by the natural rearrangement of the particles. In contrast to Eulerian methods, no interface capturing algorithms nor local mesh refinement is required. Hence, the SPH method is broadly used for simulating free surface flow configurations where the liquid motion is driven by means of gravity, inertia or pressure [5]. However, despite its advantages, SPH suffers from peculiar weaknesses. First, mostly in shear driven flows, an instability can lead to voids in the particle lattice, which in turns, lead to numerical divergence. Second, due to the motion of the particles with the fluid velocity, a disorder of the particle arrangement may be encountered, that continuously changes during the simulation and compromises the accuracy of the spatial operators. Therefore, a correction algorithm has to be applied

Email address: geoffroy.chaussonnet@kit.edu (G. Chaussonnet)

at every time step, which significantly increases the computational costs. On the other hand, it was observed by Colagrossi et al. [6] that the inaccuracy induced by the particle disorder counteracts the onset of the instability mentioned above. This phenomenon will be demonstrated analytically in the present study. Several authors investigated the stability of the SPH method. Fulk [7] extensively studied the stability in a discrete 1D configuration on a infinite domain for different sets of SPH equations. He emphasized the onset of the instability at the highest wavenumber $\pi/\Delta x$ (Δx being the inter-particle distance), when the summation of the second derivative of the kernel (W'') over the neighbors and the local pressure (P) have different signs. The author proposed many strategies to overcome this instability, such as using (i) concave up/down kernels, (ii) a background pressure or (iii) a particle motion correction. It is worth to note that the two latter tweaks are still among the most popular. At the same time, Swegle et al. [8] conducted a von-Neumann linear stability analysis (LSA) of viscous discrete 1D SPH with an equation of state (EoS) similar to the Tait's EoS. They derived their analysis by supposing only two neighbors, and they found the same condition as Fulk [7] for the onset of the instability at highest wavenumber. They finally extended the results to an arbitrary number of neighbors and found the same condition on $\sum W''$ to determine the stability. Balsara [9] conducted a von-Neumann LSA of 1D compressible SPH where different time integration schemes and different inter-particle spacings were investigated. The author derived the dispersion relation for medium to large wavelength, contrary to Fulk [7] and Swegle et al. [8] who focused on the largest wavenumber. The author advised to keep the ratio of smoothing length to inter-particle distance between 1.0 and 1.4 to minimize unrealistic acoustic wave dispersion. However, no Taylor series expansion of the kernel was taken into account, and no tensile instability was found. Morris [10] applied LSA to discrete in-space 1D smooth particles magneto-hydrodynamics (SPMHD) on an infinite domain. The author considered a weakly compressible approach and both a viscous and inviscid flow. For the first time, a non-zero background pressure was taken into account, and different approximations of the pressure gradient were investigated. The author found that the same instability as Fulk [7] for the highest wavenumber, but he attributed its origin to a negative background pressure and not depending on the product $(\sum W'') \times P$. Hence, he implied that the sum of W'' has always the same sign. He found this instability independent of the viscosity. In a similar study, Rasio [11] derived the numerical sound speed depending on several parameters, among which are the number of neighbors and the first and second derivative of the kernel. Belytschko et al. [12] proposed a unified framework to study the stability of meshless particle methods including SPH. They found new conditions of instability based on the relation between the wavenumber and the number of neighbors, and attributed it to the tensile instability found by Swegle et al. [8]. Like Morris [10], they highlighted a spurious mode at $\pi/\Delta x$ that they assigned to a rank deficiency of the stiffness matrix in the linearized equations. Børve et al. [13] applied a LSA to 2D SPMHD without background pressure in the EoS. They found too that the ratio of smoothing length to inter-particle distance should be between 1.0 and 1.4. More recently, Dehnen and Aly [14] conducted a LSA in 3D of WCSPH and showed the superiority of the Wendland kernel. They highlighted the difference between tensile and pairing instability and explored the link between negative values of the kernel Fourier transform and the pairing instability. Due to their multidimensional analysis, they were able to separate the longitudinal and transverse modes. Furthermore, they stressed the importance of the density estimator in SPH method, especially with regards to the pairing instability. Violeau and Leroy [15] performed a von-Neumann LSA on multidimensional viscous weakly-compressible SPH, with a continuous spatial scheme. Unlike the authors previously mentioned, they considered a discretized time variable, which highlighted the importance of the time integration scheme on the stability.

As pointed out by Dehnen and Aly [14], the estimation of the density is an important issue that influences the stability of SPH method. Classically, there are two different methods to estimate the density of the fluid in WCSPH. First, the density is algebraically determined by the ratio of the particle mass and its effective volume, based on the position of its neighbors [16]. This method is referred to as *sum-SPH* subsequently. Second, the density is estimated from the SPH formulation of the continuity equation [16]. This method will be referred to as *div-SPH*. Recently, a method called δ -SPH was presented by Antuono et al. [17]. It was successfully applied in the field of free surface flows [18]. It is based on div-SPH with additional dissipation terms in each of the Navier-Stokes equations, which causes the modification of the estimation of density. Finally, a method based on an artificial transport velocity formulation was developed

by Adami et al. [19]. It is referred to as *TV-SPH* in the following. Since this method is based on sum-SPH with artificially convected particles, its density estimator is different from sum-SPH.

The objectives of the present study are (i) to present a new method for the linear stability analysis of homogeneous media with the use of circulant matrices, and (ii) to apply this method to investigate the stability and the dispersion curves of the four methods for estimating the density. Note that the time variable will be considered continuous here, and the investigation of the integration scheme will be done in a subsequent study.

The traditional approach to study the stability and the dispersion of a numerical scheme is to consider perturbations as plane progressive waves (*e.g.* $\delta\phi = \epsilon e^{i(\omega t - kx)}$). The perturbations are injected into the constitutive equations and the dispersion relation is obtained by the equation $f(\omega, k) = 0$. This method is referred to as the normal mode analysis. The new method presented here makes no assumption on the shape of the perturbations. Hence, it allows non-oscillating transient solutions for the perturbations. Furthermore, as presented in the course of this paper, it is possible to derive the analytical temporal solution for each particle. The method is applied in 1D for the sake of simplicity, and still allows some findings. There is no theoretical limitations to apply this method in greater number of dimensions.

To give a synthetic view of the method, the steps are described as follows. The equations of perturbations are cast into a matrix form of an ordinary differential equation in time. Its coefficients are circulant matrices, whose eigenvalues and eigenvectors are easily obtained using the circulant matrix theory. The matrix form of the perturbations equations is then diagonalized, which corresponds to express the normal modes of the system and allow to decouple the motion of each particle. These equations are solved in the Laplace domain, which features the advantage over the Fourier transform to capture the transient state, in addition to the stability and the dispersion relation. Then, after simplification of the transfer function, the solution of the perturbation equation is transformed back into the temporal geometrical form. This temporal form is later used to validate the whole derivation against the results of the numerical resolution of the starting equation.

The plan of this paper is as follows. In Section 2, the method described above is applied to the classical sum-SPH approach, and every steps are explained thoroughly. Then the same method is applied to the div-SPH, δ -SPH and TV-SPH density estimator in Sections 3, 4 and 5, respectively. The dispersion curve of all methods, both for inviscid and viscous flows are discussed in Section 6. An illustration of the spurious mode is presented in Section 7. The expression of the perturbations equation with circulant matrices is illustrated in Appendix A, and the validation of the derivation is provided in Appendix B where the analytical temporal solutions of the perturbations are compared to the resolution by a numerical scheme.

2. Application of LSA on sum-SPH density estimator

2.1. Preliminary definitions

The 1D domain consists of N particles equidistantly placed along a segment of length L , with an inter-particle distance of Δx . This is representative of the equilibrium state (Fig. 1). In order to avoid any boundary effects, the domain is periodic. The number of neighbors on one side of the particle is labelled M . Hence, a complete sphere of influence consists of $2M + 1$ particles. The smoothing length h is chosen so that its multiple exactly covers the neighbors included in the sphere of influence as in [20]. Therefore, h , Δx and M are related by:

$$kh = (2M + 1) \Delta x = D \quad (1)$$

where k is an integer and $D = kh$ is the diameter of the sphere of influence. Due to the periodicity, the sphere of influence of particles located near the boundaries may be split into two parts located at either boundary of the domain, as illustrated on Fig. 1 (*bottom*).

In this study, two different kernels were investigated. The so-called quintic kernel [21] is defined in 1D by:

$$W(r, h) = \frac{1}{120h} \begin{cases} (3-r)^5 - 6(2-r)^5 + 15(1-r)^5 & \text{for } 0 \leq r \leq 1 \\ (3-r)^5 - 6(2-r)^5 & \text{for } 1 < r \leq 2 \\ (3-r)^5 & \text{for } 2 < r \leq 3 \end{cases} \quad (2)$$

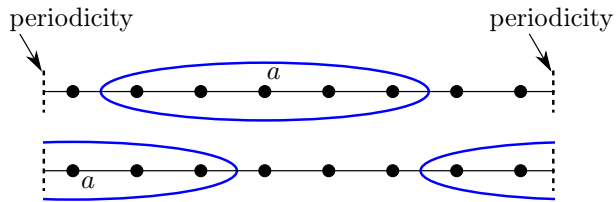


Figure 1: Top: 1D domain. Bottom: illustration of split sphere of influence

where $r = |x_a - x_b|/h$ is the normalized distance between particle a and b . The second investigated kernel belongs to the family of Wendland kernels [22]. It is expressed in 1D as:

$$W(r, h) = \frac{1}{2h} (1 - r)^5 (1 + 5r + 8r^2) \quad (3)$$

which is a seventh-order polynomial. Note that even though the fifth-order polynomial $(1 - r)^4 (1 + 4r)$ is often applied in the SPH community, its use here is inappropriate because its degree depends on the integer part of $d/2$ where d is the number of dimension, leading to a C^2 -function of degree 4 in 1D [22]. As we want to investigate kernels of at least degree 5, we dismiss the aforementioned polynomials. In the following, the kernel defined by Eq. 3 is simply referred to as the *Wendland kernel*. In this case, the particle distance is normalized by the radius of the sphere of influence $r = |x_a - x_b|/3h$.

In the rest of this paper, the dependency of the kernel on h will be dropped in the notation: $W(r) \equiv W(r, h)$ for the sake of simplicity. The radius of the sphere of influence is set constant to $3h$, which leads to discrete values of Δx (Eq. 1):

$$\Delta x = \frac{6h}{2M+1} = \frac{D}{2M+1} \quad (4)$$

Furthermore, Dehnen and Aly [14] showed that a more universal measure of the kernel characteristic length was given by its standard deviation \tilde{h} :

$$\tilde{h}^2 = \int r^2 W(r) dr \quad (5)$$

This length is equal to $h/\sqrt{2} \approx 0.707h$ and $h\sqrt{3/5} \approx 0.775h$ for the quintic and the Wendland kernel, respectively. It will be used later as the reference length scale to non-dimensionalize the equations, except with Δx when it is used to quantify the number of neighbors (Eq. 4) or the kernel compacity. In this case, the diameter of the sphere of influence D will be used.

Finally, the letter a refers to the particle under consideration whereas b refers to its neighbors. Hence \sum_b is a summation over the neighbors of particle a . The difference between a quantity at particle a and at particle b is indexed ab . For instance, $x_a - x_b$ is abbreviated by x_{ab} . For the kernel, $W(x_a - x_b)$ is abbreviated by W_{ab} . Tensor of n^{th} order are n -time underlined, e.g. \underline{V} and \underline{M} denote a vector and a matrix, respectively.

2.2. System of equations

In the absence of gravity, the 1D WCSPH approach with the algebraic density formulation (sum-SPH) is defined by the following system of equation:

$$\left\{ \begin{array}{l} \rho_a = m_a \sum_b W_{ab} \quad (6a) \\ \frac{d^2 x_a}{dt^2} = -\frac{1}{\rho_a} \sum_b V_b (p_b + p_a) W'_{ab} + 2\nu \sum_b V_b \frac{u_a - u_b}{r_{ab}} W'_{ab} \quad (6b) \\ p_a = \frac{\rho_0 c^2}{\gamma} \left[\left(\frac{\rho_a}{\rho_0} \right)^\gamma - 1 \right] + p_{back} \quad (6c) \end{array} \right.$$

In the momentum conservation (Eq. 6b), the term W'_{ab} is the derivative $\partial W_{ab}/\partial x_a$ which corresponds to the kernel gradient ∇W_{ab} in 1D. The pressure gradient is expressed by the so-called G_+ operator where the pressure p_a and p_b are added, ensuring conservation of linear momentum. The second term on the RHS of Eq. 6b represents the viscous effects. It exhibits the kinematic viscosity ν multiplied by the Laplacian of the velocity in the SPH formalism [23]. Another frequent expression of the Laplacian was proposed by Morris et al. [21], but in 1D, its expression reduces to the same as the one of Cleary and Monaghan [23]. Equation 6c is the Tait equation of state, valid for weakly compressible flows [24]. The term γ is the polytropic ratio, usually set to 7.

2.3. Linearization

The linearization of the physical variables (density, position, velocity and pressure) is written:

$$\rho = \bar{\rho} + \delta\rho, \quad x = \bar{x} + \delta x, \quad u = \bar{u} + \delta u, \quad p = \bar{p} + \delta p \quad (7)$$

where overlined quantities are constant and δX is a small perturbation of the quantity X . In the rest of the paper, the mean velocity \bar{u} is set to a constant, so that the base flow is incompressible. The particle volume V is defined as $V = m/\rho$ and linearized to the first order using Eq. 7:

$$V = m/\rho \approx \bar{V} \left(1 - \frac{\delta\rho}{\bar{\rho}} \right) \quad (8)$$

The value of the kernel is linearized by a Taylor expansion of first order as depicted in Fig. 2:

$$W(x_a - x_b) \approx W(\bar{x}_a - \bar{x}_b) + (\delta x_a - \delta x_b) W'(\bar{x}_a - \bar{x}_b) \quad (9a)$$

$$W'(x_a - x_b) \approx W'(\bar{x}_a - \bar{x}_b) + (\delta x_a - \delta x_b) W''(\bar{x}_a - \bar{x}_b) \quad (9b)$$

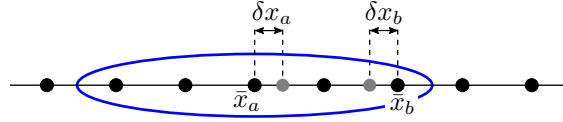


Figure 2: Linearization of the kernel

For the sake of clarity in the following, Eqs. 9 are written as:

$$W_{ab} \approx W_{ab} + \delta x_{ab} W'_{ab} \quad \text{and} \quad W'_{ab} \approx W'_{ab} + \delta x_{ab} W''_{ab} \quad (10)$$

Inserting Eqs. 7, 8 and 10 into the Eqs. 6, the linearized equations of perturbations around an equilibrium state is expressed as:

$$\left\{ \begin{array}{l} \delta\rho_a = m \sum_b (\delta x_a - \delta x_b) W'_{ab} \\ \frac{d^2 \delta x_a}{dt^2} = \bar{V} \sum_b \left[2 \frac{\bar{p}}{\bar{\rho}^2} (\delta\rho_a + \delta\rho_b) W'_{ab} - 2 \frac{\bar{p}}{\bar{\rho}} \delta x_{ab} W''_{ab} - \frac{\delta p_a + \delta p_b}{\bar{\rho}} W'_{ab} + 2\nu \frac{d}{dt} (\delta x_{ab}) \frac{W'_{ab}}{x_{ab}} \right] \\ \delta p_a = c^2 \delta\rho_a \end{array} \right. \quad (11a)$$

$$\left\{ \begin{array}{l} \frac{d^2 \delta x_a}{dt^2} = \bar{V} \sum_b \left[2 \frac{\bar{p}}{\bar{\rho}^2} (\delta\rho_a + \delta\rho_b) W'_{ab} - 2 \frac{\bar{p}}{\bar{\rho}} \delta x_{ab} W''_{ab} - \frac{\delta p_a + \delta p_b}{\bar{\rho}} W'_{ab} + 2\nu \frac{d}{dt} (\delta x_{ab}) \frac{W'_{ab}}{x_{ab}} \right] \\ \delta p_a = c^2 \delta\rho_a \end{array} \right. \quad (11b)$$

$$\left\{ \begin{array}{l} \delta p_a = c^2 \delta\rho_a \end{array} \right. \quad (11c)$$

By combining Eqs. 11b and 11c, one can express the acceleration of the perturbed particles as:

$$\frac{d^2 \delta x_a}{dt^2} = -m \sum_b \frac{\delta\rho_a + \delta\rho_b}{\bar{\rho}^2} \left[c^2 - \frac{2\bar{p}}{\bar{\rho}} \right] W'_{ab} + \frac{2\bar{p}}{\bar{\rho}^2} \delta x_{ab} W''_{ab} - 2 \frac{\nu}{\bar{\rho}} \frac{d}{dt} (\delta x_{ab}) \frac{W'_{ab}}{x_{ab}} \quad (12)$$

This equation is well-known in the literature, and was already derived, for instance by Monaghan [16]. However, we show in the following that Eqs. 11 and 12 can be further simplified. Indeed, on an ordered particle lattice, the pairwise summation of the kernel gradient for two particles b equidistant from particle a , is equal to zero. This is because the kernel gradient is an odd function. Therefore, each time that the kernel gradient is the only variable depending on b under the summation, it is can be simplified. For instance, Eq. 11a can be decomposed as:

$$\delta\rho_a = m \sum_b (\delta x_a - \delta x_b) W'_{ab} = m \delta x_a \underbrace{\sum_b W'_{ab}}_{=0 \text{ on an ordered lattice}} - m \sum_b \delta x_b W'_{ab} \quad (13)$$

So that:

$$\delta\rho_a = -m \sum_b \delta x_b W'_{ab} \quad (14)$$

Therefore, all perturbations at particle a vanish when they are multiplied by the kernel gradient, and Eqs. 11 can be simplified to:

$$\left\{ \begin{array}{l} \delta\rho_a = -m \sum_b \delta x_b W'_{ab} \\ \frac{d^2 \delta x_a}{dt^2} = \bar{V} \sum_b \left[2 \frac{\bar{p}}{\bar{\rho}^2} \delta\rho_b W'_{ab} - 2 \frac{\bar{p}}{\bar{\rho}} \delta x_{ab} W''_{ab} - \frac{\delta p_b}{\bar{\rho}} W'_{ab} + 2\nu \frac{d}{dt} (\delta x_{ab}) \frac{W'_{ab}}{x_{ab}} \right] \\ \delta p_a = c^2 \delta\rho_a \end{array} \right. \quad (15a)$$

$$\left[2 \frac{\bar{p}}{\bar{\rho}^2} \delta\rho_b W'_{ab} - 2 \frac{\bar{p}}{\bar{\rho}} \delta x_{ab} W''_{ab} - \frac{\delta p_b}{\bar{\rho}} W'_{ab} + 2\nu \frac{d}{dt} (\delta x_{ab}) \frac{W'_{ab}}{x_{ab}} \right] \quad (15b)$$

$$\delta p_a = c^2 \delta\rho_a \quad (15c)$$

The motion of particle a (Eq. 15b) depends on the perturbations of its neighbors via four different terms on the right-hand side. The first term depends on the neighbor density due to the mass conservation (Eq. 8) and represents the cross effects of compressibility and constant pressure. The second term depends on the particle distance from their equilibrium position and is proportional to the equilibrium pressure. It has no physical meanings and stems from the inaccuracy of the SPH gradient operator on disordered particle lattices. The third term results from the pressure perturbations and the last term comprises the viscous effects.

2.4. Converting the perturbation equation into a circulant matrix system

In this section the transformation of the perturbation equations (Eqs. 15) to a matrix system is explained. All perturbed variables δx , $\delta\rho$, δp of Eq. 15 are written down for all particles *i.e.* $\delta x_0, \delta x_1, \dots, \delta\rho_0, \delta\rho_1, \dots, \delta p_0, \delta p_1, \dots$ and then gathered into perturbation vectors:

$$\left\{ \begin{array}{l} \underline{X} = (\delta x_0, \delta x_1, \delta x_2, \dots, \delta x_{N-1})^T \\ \underline{R} = (\delta\rho_0, \delta\rho_1, \delta\rho_2, \dots, \delta\rho_{N-1})^T \\ \underline{P} = (\delta p_0, \delta p_1, \delta p_2, \dots, \delta p_{N-1})^T \end{array} \right. \quad (16)$$

As illustrated in Appendix A, Eqs. 15 can be expressed as a matrix system:

$$\left\{ \begin{array}{l} \underline{R} = m \underline{A}' \underline{X} \\ \frac{d^2}{dt^2} (\underline{X}) = -2 \frac{\bar{p} \bar{V}}{\bar{\rho}^2} \underline{A}' \underline{R} + 2 \frac{\bar{p} \bar{V}}{\bar{\rho}} \underline{A}'' \underline{X} + \frac{\bar{V}}{\bar{\rho}} \underline{A}' \underline{P} + 2\bar{V} \nu \underline{A}''' \frac{d}{dt} \underline{X} \\ \underline{P} = c^2 \underline{R} \end{array} \right. \quad (17a)$$

$$\frac{d^2}{dt^2} (\underline{X}) = -2 \frac{\bar{p} \bar{V}}{\bar{\rho}^2} \underline{A}' \underline{R} + 2 \frac{\bar{p} \bar{V}}{\bar{\rho}} \underline{A}'' \underline{X} + \frac{\bar{V}}{\bar{\rho}} \underline{A}' \underline{P} + 2\bar{V} \nu \underline{A}''' \frac{d}{dt} \underline{X} \quad (17b)$$

$$\underline{P} = c^2 \underline{R} \quad (17c)$$

where the matrices \underline{A}' , \underline{A}'' and \underline{A}''' enjoy interesting properties. First, \underline{A}' is antisymmetric while \underline{A}'' and \underline{A}''' are symmetric. Second, and most important for the rest of the study, all three matrices are *circulant*

matrices [25]. Therefore, they can be expressed by their first row vector, \underline{C}' , \underline{C}'' and \underline{C}''' respectively:

$$\underline{C}' = \begin{cases} c'_j = -c'_{n-j} = W'(j\Delta x) & \text{for } j \in [1, M] \\ c'_j = 0 & \text{otherwise} \end{cases} \quad (18)$$

$$\underline{C}'' = \begin{cases} c''_0 = -2 \sum_{j=1}^M W''(j\Delta x) \\ c''_j = c''_{n-j} = W''(j\Delta x) & \text{for } j \in [1, M] \\ c''_j = 0 & \text{otherwise} \end{cases} \quad (19)$$

$$\underline{C}''' = \begin{cases} c'''_0 = 2 \sum_{j=1}^M W'(j\Delta x)/(j\Delta x) \\ c'''_j = c'''_{n-j} = -W'(j\Delta x)/(j\Delta x) & \text{for } j \in [1, M] \\ c'''_j = 0 & \text{otherwise} \end{cases} \quad (20)$$

Note that in the expressions of \underline{C}' , \underline{C}'' and \underline{C}''' , the properties $W'(-j\Delta x) = -W'(j\Delta x)$ and $W''(-j\Delta x) = W''(j\Delta x)$ were used. In Eq. 17b, the pressure and density terms are multiplied by \underline{A}' while the viscous term is multiplied by \underline{A}''' . Therefore, this approach can be regarded as an expression of the linearized SPH operators in a matrix form. The linearized gradient is expressed by \underline{A}' , and the linearized Laplacian is expressed by \underline{A}''' . The matrix \underline{A}'' comes from the linearization of the gradient of a constant term. It should be zero if the SPH gradient operator was first order consistent. Note that these matrices are similar to other terms in the literature. For instance, \underline{A}'^2 and \underline{A}''' are similar to F_1 and F_2 by Violeau and Leroy [15], and to G_1 and G_2 (Section 4.1.2) by Fulk [7].

Expressing the pressure fluctuation with the help of the EoS (Eq. 6c) leads to $\bar{p} = p_{back}$. Therefore, the constant part of the pressure is the background pressure. Note that originally, the Tait EoS does not include any background pressure term. The system 17 is further simplified with $\bar{V} = \Delta x$ and $m = \bar{\rho} \Delta x$. Introducing the non-dimensional background pressure as $p_{bg} = p_{back}/\bar{\rho} c^2$ and substituting the perturbed pressure and density into Eq. 17b finally leads to:

$$\frac{d^2}{dt^2}(\underline{X}) = \Delta x c^2 [\Delta x \underline{A}'^2(1 - 2p_{bg}) + 2p_{bg} \underline{A}'''] \underline{X} + 2\nu \Delta x \underline{A}''' \frac{d}{dt}(\underline{X}) \quad (21)$$

Equation 21 can be written in a non-dimensional form using:

$$\begin{cases} \underline{X}^* = \underline{X}/\tilde{h}, & t^* = ct/\tilde{h}, & \Delta x^* = \Delta x/\tilde{h}, \\ \underline{A}'^* = \tilde{h}^2 \underline{A}', & \underline{A}''^* = \tilde{h}^3 \underline{A}'', & \underline{A}'''^* = \tilde{h}^3 \underline{A}''', & \nu^* = \nu/(\tilde{h}c) \end{cases} \quad (22)$$

It leads to:

$$\frac{1}{\Delta x} \frac{d^2}{dt^2}(\underline{X}) = [\Delta x \underline{A}'^2(1 - 2p_{bg}) + 2p_{bg} \underline{A}'''] \underline{X} + 2\nu \underline{A}''' \frac{d}{dt}(\underline{X}) \quad (23)$$

where the variables are written in their non-dimensional form without the asterisk (*) for the sake of simplicity. In the following, all variables are written in the non-dimensional form unless it is explicitly mentioned. When it is used to illustrate the number of neighbors, the non-dimensional inter particle distance will be written $\tilde{\Delta}x = \Delta x/D$. Equation 23 is a matrix ordinary differential equation where the unknown is the vector \underline{X} .

2.5. Properties of matrices \underline{A}' , \underline{A}'' and \underline{A}'''

Since matrices \underline{A}' , \underline{A}'' and \underline{A}''' are circulant matrices, they are diagonalizable in the same basis [25]. Their eigenvalues are labeled λ'_j , λ''_j and λ'''_j , respectively:

$$\lambda'_j = 2i \sum_{k=1}^M c'_k \sin\left(\frac{2\pi}{N}kj\right) \quad (24)$$

$$\lambda_j'' = c_0'' + 2 \sum_{k=1}^M c_k'' \cos\left(\frac{2\pi}{N}kj\right) \quad (25)$$

$$\lambda_j''' = c_0''' + 2 \sum_{k=1}^M c_k''' \cos\left(\frac{2\pi}{N}kj\right) \quad (26)$$

where \hat{i} is the imaginary number. These eigenvalues depend only on (i) the kernel, (ii) the total number of particles N , and (iii) the number of neighbours M . The matrix $\underline{\underline{A}}'^2$ is also a circulant matrix. Since the eigenvalues of $\underline{\underline{A}}'$ are pure imaginary, the eigenvalues of $\underline{\underline{A}}'^2$ are negative. In addition, eigenvalues are symmetric in the sense:

$$\lambda_j^2 = \lambda_{N-j}^2, \quad \lambda_j'' = \lambda_{N-j}'', \quad \lambda_j''' = \lambda_{N-j}''' \quad \text{for } j \in [1, N_{mid}] \quad (27)$$

where

$$N_{mid} = \begin{cases} (N-1)/2 & \text{for } N \text{ odd} \\ N/2 & \text{for } N \text{ even} \end{cases} \quad (28)$$

Furthermore, the eigenvalues exhibit particular values for the mode $j=0$ with $\lambda_0' = \lambda_0'' = \lambda_0''' = 0$. At the largest mode $j = N/2$, $\lambda_{N/2}'$ is equal to zero, meaning that matrix $\underline{\underline{A}}'$ has a rank deficiency that may lead to spurious modes [12]. As highlighted by Fulk [7], the eigenvalue of $\underline{\underline{A}}''$ for the largest mode is different from zero, *i.e.* $\lambda_{N/2}'' \neq 0$. Furthermore, it is found in the present study that the eigenvalue of $\underline{\underline{A}}'''$ at the largest mode is also non-zero, $\lambda_{N/2}''' \neq 0$. Finally, the eigenvalues of a circulant matrix are equal to the coefficients of the discrete Fourier transform of the its first row [25]. Hence, λ_j' , λ_j'' and λ_j''' are the coefficients of the discrete Fourier transform of $W'(x)$, $W''(x)$ and $W'(x)/x$, respectively. Violeau et al. [26] approximated λ_i''' for a large number of particles whereas it is expressed exactly in the present study, independently of the number of particles.

Figure 3 shows an illustration of the eigenvalues, for $N=63$, $M=3$ (*i.e.* $\tilde{\Delta}x=0.14$) and different kernels. It is observed that all eigenvalues are always negative. At largest modes, λ_i^2 goes to zero whereas the other

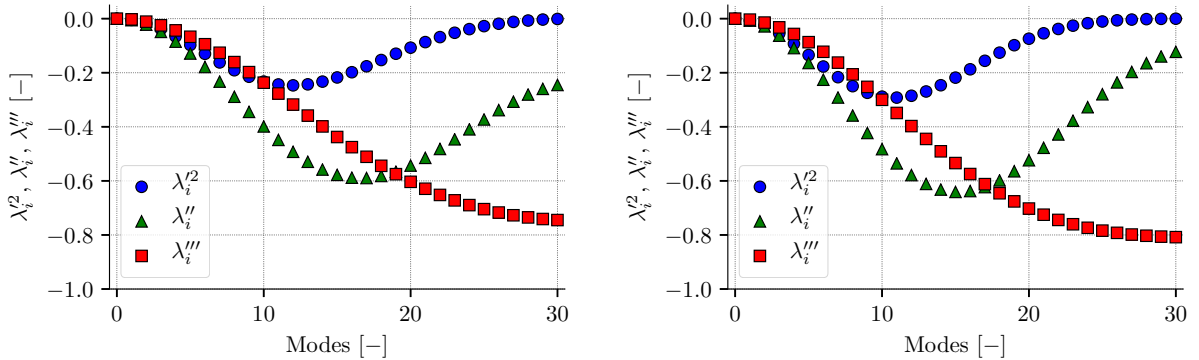


Figure 3: Values of $(\lambda_i^2, \lambda_i'', \lambda_i''')$ for $N=63$ and $\tilde{\Delta}x=0.14$. Left: quintic kernel. Right: Wendland kernel.

values remain significantly negative.

2.6. Projection in the modal space

Since $\underline{\underline{A}}'^2$, $\underline{\underline{A}}''$ and $\underline{\underline{A}}'''$ are circulant matrices, they can be diagonalized on the same basis. By expressing $\underline{\underline{A}}'^2$, $\underline{\underline{A}}''$ and $\underline{\underline{A}}'''$ as diagonal matrices:

$$\underline{\underline{A}}'^2 = \underline{\underline{P}}^{-1} \underline{\underline{\Delta}}'^2 \underline{\underline{P}} \quad \text{and} \quad \underline{\underline{A}}'' = \underline{\underline{P}}^{-1} \underline{\underline{\Delta}}'' \underline{\underline{P}} \quad \text{and} \quad \underline{\underline{A}}''' = \underline{\underline{P}}^{-1} \underline{\underline{\Delta}}''' \underline{\underline{P}} \quad (29)$$

and defining $\underline{Y} = \underline{P}\underline{X}$, Eq. 23 is expressed:

$$\frac{1}{\Delta x} \frac{d^2}{dt^2}(\underline{Y}) = [\Delta x \underline{\Delta}^{\prime 2} + 2p_{bg}(\underline{\Delta}'' - \Delta x \underline{\Delta}^{\prime 2})] \underline{Y} + 2\nu \underline{\Delta}''' \frac{d}{dt}(\underline{Y}) \quad (30)$$

As $\underline{\Delta}^{\prime 2}$, $\underline{\Delta}''$ and $\underline{\Delta}'''$ are diagonal matrices composed of the eigenvalues, Eq. 30 can be reduced to $N_{mid} + 1$ non-coupled ordinary differential equations:

$$\frac{1}{\Delta x} \frac{d^2}{dt^2}(y_i) - 2\nu \lambda_i''' \frac{d}{dt}(y_i) - [\Delta x \lambda_i^{\prime 2} + 2p_{bg}(\lambda_i'' - \Delta x \lambda_i^{\prime 2})] y_i = 0 \quad (31)$$

with i being the mode number and $i \in \llbracket 0, N_{mid} \rrbracket$. Hence, Eq. 31 represents the perturbations expressed in the *modal space*. Furthermore, the change-of-basis rules from the matrix \underline{A}' to its eigenvalue is the classical definition of a discrete Fourier transform [25]. This means that expressing the equation of motion in the modal space is equivalent to apply a discrete spatial Fourier transform. Thus, studying the stability of SPH with λ_j' , λ_j'' and λ_j''' is equivalent to study the values of the discrete Fourier transform of the different expressions involving the kernel derivatives. This result is similar to those of (i) Fulk [7] and Swegle et al. [8] because it involves derivatives of the kernel, and similar to those of Dehnen and Aly [14] because it involves the Fourier transform of the kernel, here in the discrete form. Equation 31 also shows the influence of the modes of $W'(x)/x$ represented by λ_i''' . Equation 31 is formally rewritten as:

$$\frac{d^2}{dt^2}(y_i) + \sigma_i \frac{d}{dt}(y_i) + \phi_i^2 y_i = 0 \quad (32)$$

with

$$\sigma_i = -2\nu \Delta x \lambda_i''' \quad \text{and} \quad \phi_i^2 = -\Delta x^2 \lambda_i^{\prime 2} - 2\Delta x p_{bg}(\lambda_i'' - \Delta x \lambda_i^{\prime 2}) \quad (33)$$

In the following, the two terms appearing in the expression of ϕ_i^2 are labeled $\psi_{1,i}$ and $\psi_{2,i}$, and they are given by:

$$\psi_{1,i} = (\Delta x \lambda_i')^2 (1 - 2p_{bg}) \quad \text{and} \quad \psi_{2,i} = 2p_{bg} \Delta x \lambda_i'' \quad (34)$$

Note that these terms resemble to those labeled D_1 and D_2 (Section 4.1.2) by Fulk [7]. However, D_1 and D_2 were defined with an infinite summation so they cannot be numerically determined. In the present study, $\psi_{1,i}$ and $\psi_{2,i}$ are exactly determined by a summation from 1 to M .

Equation 32 is an ordinary differential equation of second order with a damping term σ_i and an undamped angular frequency ϕ_i . Some values of the damping factor σ_i are plotted in Fig. 4 for $N=1000$ and $\nu=1$, with different Δx . The values are always positive, ensuring a damping for any selection of the parameters. It was observed (but not presented here) that σ_i is very little dependent on the type of kernel. It can be shown that the asymptote of the damping term in Fig. 4 for high modes is given by:

$$\lim_{\substack{N \rightarrow \infty \\ M \rightarrow \infty}} \sigma_{N/2} = \int_{\Omega} \frac{W'(x)}{x} dx \quad (35)$$

In contrast, ϕ_i^2 shows a more complex behavior with regards to p_{bg} , Δx and the type of kernel. A map of ϕ_i^2 is shown in Fig. 5, for a larger number of particles ($N=10000$), $p_{bg} = 1$, and different number of neighbors M . First, ϕ_i^2 is always ≥ 0 , implying that ϕ_i is real. Hence, any onset of linear instability will be cancelled. However, for the quintic kernel, when $M \geq 9$ (*i.e.* below $\Delta x \leq 0.32$), some modes lower than N_{mid} lead to $\phi_i^2=0$, generating a spurious mode which may trigger marginal instabilities at certain conditions. Such particular values are not observed with the Wendland kernel, suggesting at better stability.

2.6.1. Effect of the background pressure on the particle disorder

This subsection details the effect of background pressure on one single particle and demonstrates the reordering effect of background pressure. Considering only the contribution of the background pressure to the acceleration of the perturbation (Eq. 31), one obtains:

$$\frac{d^2 y_i}{dt^2} = 2p_{bg}(\lambda_i'' - \Delta x \lambda_i^{\prime 2}) \Delta x y_i \quad (36)$$

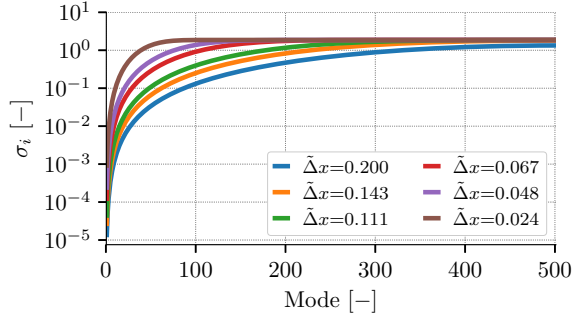


Figure 4: Values of σ_i for $N=1000$, $\nu=1$, $p_{bg} = 1$, quintic kernel and different $\tilde{\Delta}x$.

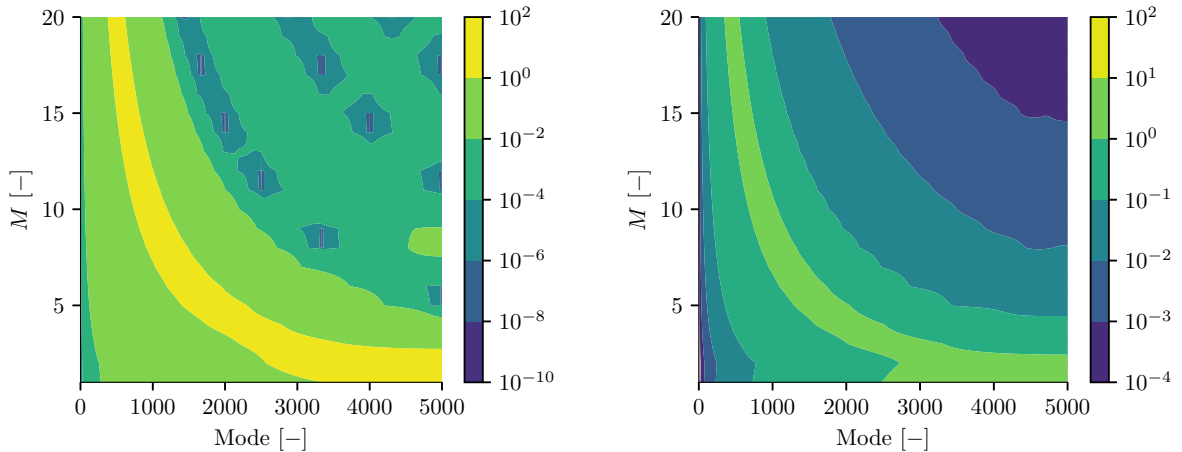


Figure 5: Color map of ϕ_i^2 for $N=10000$, $p_{bg} = 1$. Left: quintic kernel. Right: Wendland kernel.

Equation 36 states that the contribution of the background pressure to the acceleration of any perturbation is of the sign of the term between bracket $\varphi_i = \lambda_i'' - \Delta x \lambda_i'^2$. This term depends on Δx and on the type of kernel. Figure 6 shows its dependence on Δx for the quintic and Wendland kernel. The crosses in Fig. 6 correspond to negative values that could not be shown in a log-log plot. Hence, the y position of crosses corresponds to φ_i instead of $-\varphi_i$. They show the presence of positive values for lower modes, both for the quintic and the Wendland kernels. These positive values are discussed in the following subsection. Apart from the points indicated by the crosses, φ_i is always negative, meaning that the acceleration due to the background pressure is acting against the perturbation, which demonstrates the reordering effect of the background pressure. This results was observed by Colagrossi et al. [6], Marrone et al. [18], and Litvinov et al. [27], but to the authors knowledge, there was no formal proof of the feature. According to Eq. 36, the time scales associated with the reordering effect of background pressure are: $\tau_{bg} = 1/\sqrt{2p_{bg}\Delta x(\lambda_i'' - \Delta x \lambda_i'^2)}$.

2.6.2. Critical value of the background pressure

The term φ_i is positive (crosses in Fig. 6) for lower modes, which corresponds to large wavelength as it will be shown in Section 2.8. This means that the background pressure can increase the disorder for low frequency perturbations and particular values of $\tilde{\Delta}x$ (or M , equivalently). As shown in Fig. 5, for usual values of the background pressure, no instability is found ($\phi_i^2 > 0$), but for a background pressure above a critical value, the term proportional to p_{bg} is dominant in ϕ_i^2 (Eq. 33), and ϕ_i^2 becomes negative. Searching

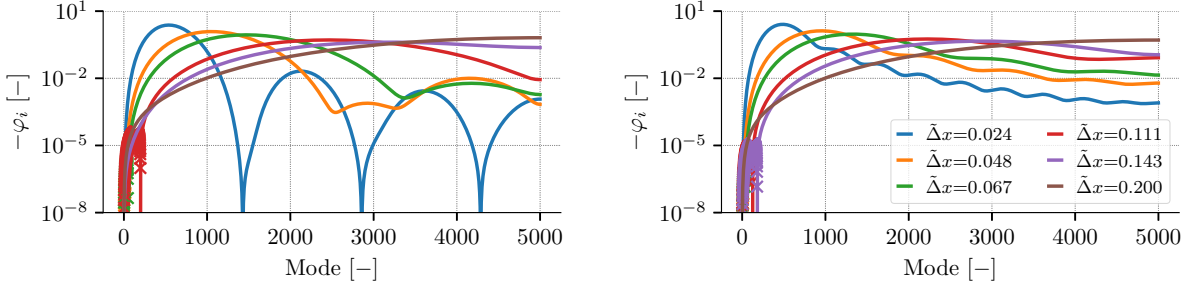


Figure 6: Values of $-\varphi_i$ for $N=10000$ with quintic (left) and Wendland (right) kernel.

the critical p_{bg} such as $\phi_i^2 < 0$ and $\varphi_i > 0$ leads to:

$$p_{bg} > \frac{1}{2} \frac{\Delta x \lambda_i'^2}{\Delta x \lambda_i'^2 - \lambda_i''} \quad (37)$$

The critical values of p_{bg} are plotted in Fig. 7 for $N=10000$ and different $\tilde{\Delta}x$. Only the lower modes are subject to the instability, and therefore admit a critical background pressure. It is interesting to note that the Wendland kernel is also impacted by this instability. Contrary to the instabilities that may be triggered by the spurious mode (Fig. 5), which appears for a large number of neighbors, this instability occurs also at low M . The results of this subsection and Eq. 37 are validated with numerical simulations in Appendix C.

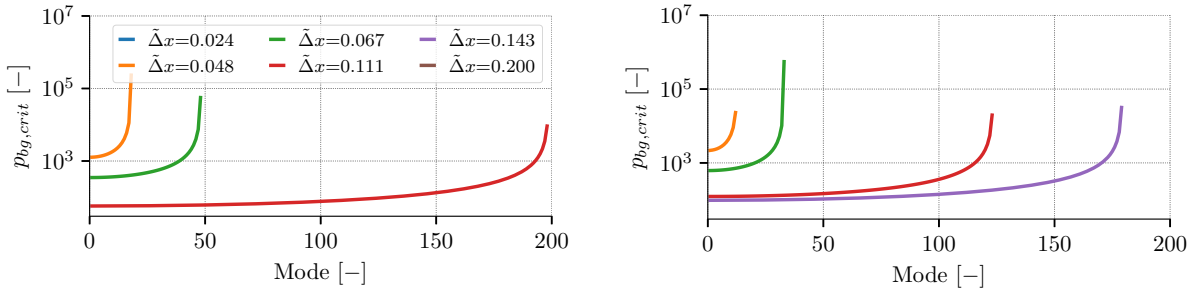


Figure 7: Critical values of p_{bg} for $N=10000$ with quintic (left) and Wendland (right) kernel.

2.7. Solutions of the perturbation equation

This subsection aims to solve the equation of perturbation for the general case. It is organized as follows: the equations are transformed into the Laplace domain, where the transient and steady state as well as the stability can be investigated. Another advantage of the Laplace domain is to express ordinary differential equations by polynomials, which simplifies the analysis. Indeed, other WSPH methods are ruled by a system of differential equations that cannot be directly integrated. After a simplification of the rational function, the solution are converted back into a temporal form of the modal space. Finally, the perturbations are written in the original geometric space.

2.7.1. Projection into the Laplace domain

Equation 32 is transformed into a Laplace formulation. The rules of Laplace transformations are:

$$\mathcal{L}(y_i) = Y_i, \quad \mathcal{L}\left(\frac{dy_i}{dt}\right) = p Y_i - y_{i,0} \quad \text{and} \quad \mathcal{L}\left(\frac{d^2 y_i}{dt^2}\right) = p^2 Y_i - p y_{i,0} - y'_{i,0} \quad (38)$$

where $y_{i,0}$ and $y'_{i,0}$ are the initial perturbation of position and velocity, respectively. The term p is the Laplace variable and must not be mistaken for the pressure term. In the Laplace domain, the perturbation of positions (Eq. 32) is given by:

$$Y_i = \frac{p + \sigma_i}{p^2 + \sigma_i p + \phi_i^2} y_{i,0} + \frac{1}{p^2 + \sigma_i p + \phi_i^2} y'_{i,0} \quad (39)$$

Hence, Y_i depends on two polynomials in p proportional to the initial perturbations. Their poles determine the stability of the system. The discriminant of the denominator is:

$$\Delta_i = \sigma_i^2 - 4\phi_i^2 \quad (40)$$

and the poles yield:

$$\pi_i^\pm = \frac{-\sigma_i}{2} \left(1 \pm \sqrt{1 - 4(\phi_i/\sigma_i)^2} \right) \quad (41)$$

The real part of π_i^\pm is always of the sign of $-\sigma_i$, (*i.e.* the sign of λ_i''') because the square root in Eq. 41 is either imaginary or lower than one. This is always true when the background pressure is positive. This implies that all modes will be damped in time, so that no instability is present, even when Δ_i becomes positive. However, even though the real part of π_i^\pm remains negative, it can be very close to zero, leading to an insufficient damping of the perturbation and a spurious mode may arise.

2.7.2. Temporal solution in the modal space

In order to transform the solution back into the temporal modal space, the denominator of the polynomials in Eq. 39 are written as:

$$p^2 + \sigma_i p + \phi_i^2 = \left(p + \frac{\sigma_i}{2} \right)^2 + \omega_i^2 \quad \text{with} \quad \omega_i^2 = -\frac{\Delta_i}{4} = \phi_i^2 - \frac{\sigma_i^2}{4} \quad (42)$$

so that Eq. 39 can be expressed as:

$$Y_i = \left[\frac{p + \sigma_i/2}{(p + \sigma_i/2)^2 + \omega_i^2} + \frac{\sigma_i}{2\omega_i} \frac{\omega_i}{(p + \sigma_i/2)^2 + \omega_i^2} \right] y_{i,0} + \left[\frac{1}{\omega_i} \frac{\omega_i}{(p + \sigma_i/2)^2 + \omega_i^2} \right] y'_{i,0} \quad (43)$$

If Δ_i is negative, then ω_i^2 is positive. Applying the inverse Laplace transform rules leads to:

$$\begin{cases} y_i(t) = f_i(t) y_{i,0} + g_i(t) y'_{i,0} & \text{with} & (44a) \\ f_i(t) = \exp\left(-\frac{\sigma_i}{2}t\right) \left[\cos(\omega_i t) + \frac{\sigma_i}{2\omega_i} \sin(\omega_i t) \right] & (44b) \\ g_i(t) = \exp\left(-\frac{\sigma_i}{2}t\right) \left[\frac{1}{\omega_i} \sin(\omega_i t) \right] & (44c) \end{cases}$$

When $\Delta_i > 0$, the solution is obtained by replacing the sine and cosine functions by their hyperbolic expressions. When $\Delta_i=0$, which is equivalent to $\omega_i=0$, then $f_i(t)$ and $g_i(t)$ reduce to:

$$f_i(t) = \exp\left(-\frac{\sigma_i}{2}t\right) \left[1 + \frac{\sigma_i}{2}t \right] \quad \text{and} \quad g_i(t) = t \exp\left(-\frac{\sigma_i}{2}t\right) \quad (45)$$

which correspond to a spurious mode. When $\nu > 0$, this mode is damped. However, in Eq. 45, $g_i(t)$ has a maximum at $t = 2/\sigma_i$ which is equal to $2/(\sigma_i e)$. This might cause instabilities in case of small damping ratio. When $\nu=0$, the spurious mode is characterized by $f_i(t)=1$ and $g_i(t)=t$. Hence, any initial perturbation of velocity grows linearly with time.

Finally, the zero mode ($i = 0$) is similar to a non-damped spurious mode:

$$f_0(t) = 1 \quad \text{and} \quad g_0(t) = t \quad (46)$$

Therefore, an initial perturbation of the velocity always leads to a constant velocity of all the particles. This is related to the conservation of linear momentum as illustrated in the next subsection. It is interesting to note that the stability of the system depends also on which physical value is perturbed.

2.7.3. Temporal solution in the geometrical space

The matrix $\underline{Y}(t)$ in Eq. 30 is a diagonal matrix whose diagonal elements are the right hand side of Eq. 44a. Multiplying $\underline{Y}(t)$ on the left by \underline{P}^{-1} leads to the expression of \underline{X} :

$$\underline{X}(t) = \underline{F}(t) \underline{X}_0 + \underline{G}(t) \underline{U}_0 \quad (47)$$

where \underline{X}_0 and \underline{U}_0 are the vector of initial perturbations for the position and velocity, respectively. The terms $\underline{F}(t)$ and $\underline{G}(t)$ are time-dependent matrices expressed by their general term:

$$F_{ij}(t) = \frac{1}{N} \left[f_0(t) + 2 \sum_{k=1}^{N_{mid}} f_k(t) \cos \left(\frac{2\pi}{N} k(i-j) \right) \right] \quad (48a)$$

$$G_{ij}(t) = \frac{1}{N} \left[g_0(t) + 2 \sum_{k=1}^{N_{mid}} g_k(t) \cos \left(\frac{2\pi}{N} k(i-j) \right) \right] \quad (48b)$$

Equations 48 highlights the coupling between the temporal solutions and the nodal oscillations. On the other hand, if only the position of the particle i is perturbed, then its own response is given by $\delta x_i(t) = F_{ii}(t) \delta x_0$ which is a pure combination of time-oscillations independent of the oscillations of the neighbors.

Let us consider an initial velocity perturbation of δu_0 applied to the particle 0 with $\nu > 0$. After a long time, due to the damping (Eq. 44c), all $g_k(t)$ are zero except $g_0(t) = t$. Therefore, the position of each particle follow the same law $\delta x_i = \delta u_0 t / N$ which means a constant momentum of $m \delta u_0 / N$. After summing the velocity of all particles, one obtains $m \delta u_0$ which corresponds to the initial momentum of the system. Consequently the linear momentum of the system is conserved. The validation of Eqs. 44 and 48 is given in Appendix B.

2.8. Towards the dispersion relation

As of now it was not possible to derive any dispersion equation because no wavelength was present in the equation of motion. However, it is possible to find a link between the time oscillations and the spatial modes by considering an initial spatial sinusoidal perturbation of mode p :

$$\delta x_{i,0} = \delta_0 \cos \left(\frac{2\pi}{N} p i \right) \quad (49)$$

where δ_0 is the amplitude of the perturbation. Because of the aliasing effect, the largest mode that can be resolved on the particle lattice is N_{mid} . Thus, $p \in \llbracket 0, N_{mid} \rrbracket$. The wavelength associated to mode p is $\lambda_p = L/p$ where $L = N \Delta x$ is the total length of the domain. Therefore, the initial sinusoidal perturbation can be written in terms of λ_p :

$$\delta x_{i,0} = \delta_0 \cos \left(2\pi i \frac{\Delta x}{\lambda_p} \right) \quad (50)$$

and the smallest resolved wavelength is $\lambda_{min} = 2\Delta x$ if N is even. Figure 8 shows an illustration of different initial sinusoidal perturbations.

Given these initial perturbations, the motion of particle i is given by:

$$\delta x_i(t) = \sum_{j=0}^{N-1} F_{ij}(t) \delta x_{j,0} \quad (51)$$

which simplifies, after some algebra, to:

$$\delta x_i(t) = f_p(t) \delta x_{i,0} \quad (52)$$

where f_p is given by Eq. 44b. This means that when a particle lattice is excited with by a spacial mode p , the particles will oscillate with the corresponding temporal mode p . Therefore, Eq. 52 establishes a link between spatial and temporal modes, *i.e.* a dispersion relation which will be investigated in Section 6.

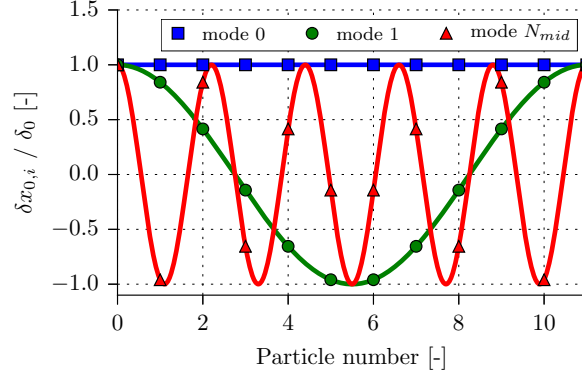


Figure 8: Illustration of different initial sinusoidal perturbations for $N=11$.

3. Application of LSA to div-SPH

In this section the motion of perturbations with div-SPH will be investigated, *i.e.* when the density is estimated with the divergence of the velocity. The equations of motion are:

$$\begin{cases} \frac{d\rho_a}{dt} = \rho_a \sum_b V_b (u_a - u_b) W'_{ab} & (53a) \\ \frac{d^2 x_a}{dt^2} = -\frac{1}{\rho_a} \sum_b V_b (p_b + p_a) W'_{ab} + 2\nu_a \sum_b V_b \frac{u_a - u_b}{r_{ab}} W'_{ab} & (53b) \\ p_a = \frac{\rho_0 c^2}{\gamma} \left[\left(\frac{\rho_a}{\rho_0} \right)^\gamma - 1 \right] + p_{back} & (53c) \end{cases}$$

which leads, after linearization, non-dimensionalization and projection into the mode basis, to:

$$\begin{cases} \frac{dz_i}{dt} = \Delta x \lambda'_i \frac{dy_i}{dt} & (54a) \\ \frac{d^2 y_i}{dt^2} = \psi_{2,i} y_i - \sigma_i \frac{dy_i}{dt} + \frac{\psi_{1,i}}{\Delta x \lambda'_i} z_i & (54b) \end{cases}$$

where σ_i , $\psi_{1,i}$ and $\psi_{2,i}$ are defined by Eqs. 33 and 34. The term z_i is the general term of the density perturbations vector in the modal space $\underline{Z} = \underline{P}\underline{R}$. The system is transformed into the Laplace domain:

$$\begin{cases} pZ_i - z_{i,0} = \Delta x \lambda'_i (pY_i - y_{i,0}) & (55a) \\ p^2 Y_i - p y_{i,0} - y'_{i,0} = \psi_{2,i} Y_i - \sigma_i (pY_i - y_{i,0}) + \frac{\psi_{1,i}}{\Delta x \lambda'_i} Z_i & (55b) \end{cases}$$

where $Y_i(p)$ and $Z_i(p)$ are the Laplace transforms of $y_i(t)$ and $z_i(t)$. The initial conditions of position, velocity and density are denoted by $y_{i,0}$, $y'_{i,0}$ and $z_{i,0}$, respectively. Substituting Eq. 55a into Eq. 55b leads to:

$$Y_i = P_1(p) y_{i,0} + P_2(p) y'_{i,0} + P_3(p) z_{i,0} \quad \text{with} \quad (56a)$$

$$P_1(p) = [p^2 + \sigma_i p - \psi_{1,i}] / Q(p) \quad (56b)$$

$$P_2(p) = p / Q(p) \quad (56c)$$

$$P_3(p) = (\psi_{1,i} / \Delta x \lambda'_i) / Q(p) \quad (56d)$$

$$Q(p) = p[p^2 + \sigma_i p + \phi_i^2] \quad (56e)$$

The poles of P_1, P_2, P_3 are the roots of $Q(p)$. They are given by:

$$r_1 = 0 \quad \text{and} \quad r_{2,3} = \frac{-\sigma_i}{2} \left(1 \pm \sqrt{1 - 4(\phi_i/\sigma_i)^2} \right) \quad (57)$$

The roots $r_{2,3}$ are equal to π_i^\pm as given by Eq. 41 with sum-SPH. Hence, their real part is either negative or zero, leading to a decreasing exponential or continuous component in the temporal domain, as for sum-SPH. In addition, the value $p = 0$ is also a pole of P_1 and P_3 , which means that the decomposition of P_1 and P_3 into rational functions will exhibit the term $1/p$. The inverse Laplace transform of $1/p$ is the Heaviside function, *i.e.* a continuous component signal. In other words, an initial perturbation of position or density will remain unaffected.

Since the the roots of Q are the same as π_i^\pm , it means that, apart from the continuous mode, the dispersion and the damping curves of div-SPH are the same as for sum-SPH. Also, the div-SPH method is subject to the critical background pressure instability highlighted in Section 2.6.2. Hence, the only particularity of using the velocity divergence to estimate the density is the non-damped perturbation of position and density.

The rational functions P_1, P_2 and P_3 are simplified to apply the inverse Laplace transforms:

$$\left\{ \begin{array}{l} P_1 = -\frac{1}{\phi_i^2} \left(\psi_{1,i} \frac{1}{p} + \psi_{2,i} \frac{p + \sigma_i/2}{(p + \sigma_i/2)^2 + \omega_i^2} + \frac{\psi_{2,i} \sigma_i}{2 \omega_i} \frac{\omega_i}{(p + \sigma_i/2)^2 + \omega_i^2} \right) \end{array} \right. \quad (58a)$$

$$\left\{ \begin{array}{l} P_2 = \frac{1}{\omega_i} \frac{\omega_i}{(p + \sigma_i/2)^2 + \omega_i^2} \end{array} \right. \quad (58b)$$

$$\left\{ \begin{array}{l} P_3 = \frac{-\psi_{1,i}}{\Delta x \lambda'_i \phi_i^2} \left(\frac{p + \sigma_i/2}{(p + \sigma_i/2)^2 + \omega_i^2} + \frac{\sigma}{2 \omega_i} \frac{\omega_i}{(p + \sigma_i/2)^2 + \omega_i^2} - \frac{1}{p} \right) \end{array} \right. \quad (58c)$$

where ω_i is defined in Eq. 42. The rational functions P_1, P_2 and P_3 are then transformed into a temporal form to $f_i(t), g_i(t), h_i(t)$, respectively. When Δ_i (Eq. 40) is negative, the functions can be expressed as :

$$\left\{ \begin{array}{l} f_i(t) = -\frac{1}{\phi_i^2} \left[\psi_{1,i} + \psi_{2,i} \exp\left(\frac{-\sigma_i}{2}t\right) \left(\cos(\omega_i t) + \frac{\sigma_i}{2 \omega_i} \sin(\omega_i t) \right) \right] \end{array} \right. \quad (59a)$$

$$\left\{ \begin{array}{l} g_i(t) = \frac{1}{\omega_i} \exp\left(\frac{-\sigma_i}{2}t\right) \sin(\omega_i t) \end{array} \right. \quad (59b)$$

$$\left\{ \begin{array}{l} h_i(t) = \frac{-\psi_{1,i}}{\Delta x \lambda'_i \phi_i^2} \left[\exp\left(\frac{-\sigma_i}{2}t\right) \left(\cos(\omega_i t) + \frac{\sigma_i}{2 \omega_i} \sin(\omega_i t) \right) - 1 \right] \end{array} \right. \quad (59c)$$

When $\Delta_i > 0$, the sinusoidal functions are to be replaced by their hyperbolic variants. When $\Delta_i = 0$, the cosine is replaced by 1 and $\sin(\omega_i t)/\omega_i$ is replaced by t . The zero mode are $f_0(t) = 1, g_0(t) = t$ and $h_0(t) = 0$. Note that $h_i(t)$ is a pure imaginary function due to the term λ'_i in its prefactor. The solution of the perturbation equation in the modal space yields:

$$y_i(t) = f_i(t) y_{i,0} + g_i(t) y'_{i,0} + h_i(t) z_{i,0} \quad (60)$$

Transforming $y_i(t)$ to $\underline{X}(t)$ is done using Eqs. 48 for the position and velocity. For the density, due to the property $\lambda'_k = -\lambda'_{n-k}$, the inverse transformation of $h_i(t)$ is:

$$H_{ij}(t) = \frac{1}{N} \left[h_0(t) + 2 \hat{i} \sum_{k=1}^{N_{mid}} h_k(t) \sin\left(\frac{2\pi}{N} k(i-j)\right) \right] \quad (61)$$

which is a real function given that $h_k(t)$ are purely imaginary. Equations. 59 and 61 are validated in Appendix B.

4. Application of LSA to δ -SPH

The same analysis is now applied to δ -SPH. This scheme, originally proposed by Antuono et al. [17], is based on div-SPH, in which additional diffusion terms are added in the density and energy equation. The equations of motion are recalled in 1D:

$$\left\{ \begin{array}{l} \frac{d\rho_a}{dt} = \rho_a \sum_b V_b (u_a - u_b) W'_{ab} + \xi hc \sum_b V_b \psi_{ab} W'_{ab} \\ \rho_a \frac{d^2 x_a}{dt^2} = - \sum_b V_b (p_b + p_a) W'_{ab} + \alpha hc \bar{\rho} \sum_b V_b \pi_{ab} W'_{ab} \\ \rho_a \frac{de_a}{dt} = p_a \sum_b V_b (u_a - u_b) W'_{ab} - \frac{\alpha hc \bar{\rho}}{2} \sum_b V_b \pi_{ab} (u_a - u_b) W'_{ab} + \chi hc \bar{\rho} \sum_b V_b \phi_{ab} W'_{ab} \\ p_a = c^2 (\rho_a - \bar{\rho}) \left[1 + \Gamma \left(\frac{e_a}{\bar{e}} - 1 \right) \right] + p_{back} \end{array} \right. \quad \begin{array}{l} (62a) \\ (62b) \\ (62c) \\ (62d) \end{array}$$

where:

$$\psi_{ab} = 2 \frac{\rho_a - \rho_b}{x_{ab}} \quad \phi_{ab} = 2 \frac{e_a - e_b}{x_{ab}} \quad \pi_{ab} = \frac{u_a - u_b}{x_{ab}} \quad (63)$$

The system of equations 62 shows, in order of appearance, the conservation of mass, momentum and energy, and the EoS. The terms α , ξ , χ and Γ are the non-dimensional coefficients of (i) the viscosity (equal to 2ν), (ii) the mass diffusivity, (iii) the energy diffusivity and (iv) the internal energy response to compressibility, respectively. In their original paper, Antuono et al. [17] omitted the background pressure in the EoS but later publications (*e.g.* Marrone et al. [18]) reintroduced it. The intermediate quantities are linearized the first-order approximation as:

$$\psi_{ab} \approx 2 \frac{\delta\rho_a - \delta\rho_b}{x_{ab}} \quad \phi_{ab} \approx 2 \frac{\delta e_a - \delta e_b}{x_{ab}} \quad \psi_{ab} \approx \frac{\delta u_a - \delta u_b}{x_{ab}} \quad (64)$$

As mentioned by Antuono et al. [17], the energy contribution inside the equation of state (Eq. 62d) is second order, so it does not appear in the density and motion equation after linearization. Non-dimensionalization and projection into the mode basis lead to the following system:

$$\left\{ \begin{array}{l} \frac{dz_i}{dt} = \Delta x \lambda'_i \frac{dy_i}{dt} + 2\Delta x \xi \lambda_i''' z_i \\ \frac{d^2 y_i}{dt^2} = \psi_{2,i} y_i - \sigma_i \frac{dy_i}{dt} + \frac{\psi_{1,i}}{\Delta x \lambda'_i} z_i \end{array} \right. \quad \begin{array}{l} (65a) \\ (65b) \end{array}$$

where, in this case, the term σ_i defined in Eq. 33 is now equal to $-\alpha \Delta x \lambda_i'''$. It is worth to note that this system of equations differs from the system of div-SPH (Eqs. 54) in that a diffusion term is added in the density equation. Translating this system into the Laplace domain and expressing the particle motion Y_i leads to:

$$Y_i = P_1(p) y_{i,0} + P_2(p) y'_{i,0} + P_3(p) z_{i,0} \quad \text{with} \quad (66a)$$

$$P_1(p) = [p^2 - (\alpha + 2\xi) \Delta x \lambda_i''' p + 2\alpha \xi (\Delta x \lambda_i''')^2 - \psi_{1,i}] / Q(p) \quad (66b)$$

$$P_2(p) = (p - 2\xi \Delta x \lambda_i''') / Q(p) \quad (66c)$$

$$P_3(p) = (\psi_{1,i} / \Delta x \lambda'_i) / Q(p) \quad (66d)$$

and

$$Q(p) = p^3 - (\alpha + 2\xi) \Delta x \lambda_i''' p^2 + [2\alpha \xi (\Delta x \lambda_i''')^2 + \phi_i^2] p + 4\Delta x^2 \xi p_{bg} \lambda_i'' \lambda_i''' \quad (67)$$

In this case, the roots of $Q(p)$ cannot be analytically expressed in a compact form. However, it is worth to note that because of the constant term $4\Delta x^2 \xi p_{bg} \lambda_i'' \lambda_i'''$, $p = 0$ is not a root of Q , which means that no

undamped continuous mode can be found, provided that both ξ and p_{bg} are non zero. Consequently, for $\xi > 0$ and $p_{bg} > 0$, any initial perturbation of any physical type is damped. This is a clear advantage of δ -SPH over div-SPH when background pressure is added. In order to investigate the poles of P_1 , P_2 and P_3 , the equation $Q(p) = 0$ is solved numerically and the roots are discussed below.

Figure 9 shows the roots of Q for different parameters. Their real part represents the stability while the imaginary part is the angular frequency of the oscillation. When the viscosity increases (Fig. 9 right), a second regime is observed for higher modes. It is an aperiodic regime where one of the damping ratio decreases to zero (r_1 in Fig. 9 right), as also pointed out by Antuono et al. [28]. In this case, the continuous solution (r_3) is damped faster than the sinusoidal modes. This means that physical oscillations have a larger amplitude than the unphysical continuous perturbations in δ -SPH. It was also observed (but not illustrated here) that when $\xi > \alpha/2$, the real part of r_1 and r_2 becomes positive for the first modes, leading to the slow divergence of a perturbation of large wavelength. The value of $\xi = \alpha/2$ was found by Antuono et al. [17] as an optimal value, but not a limiting one, probably due to the assumption of zero background pressure in their analysis.

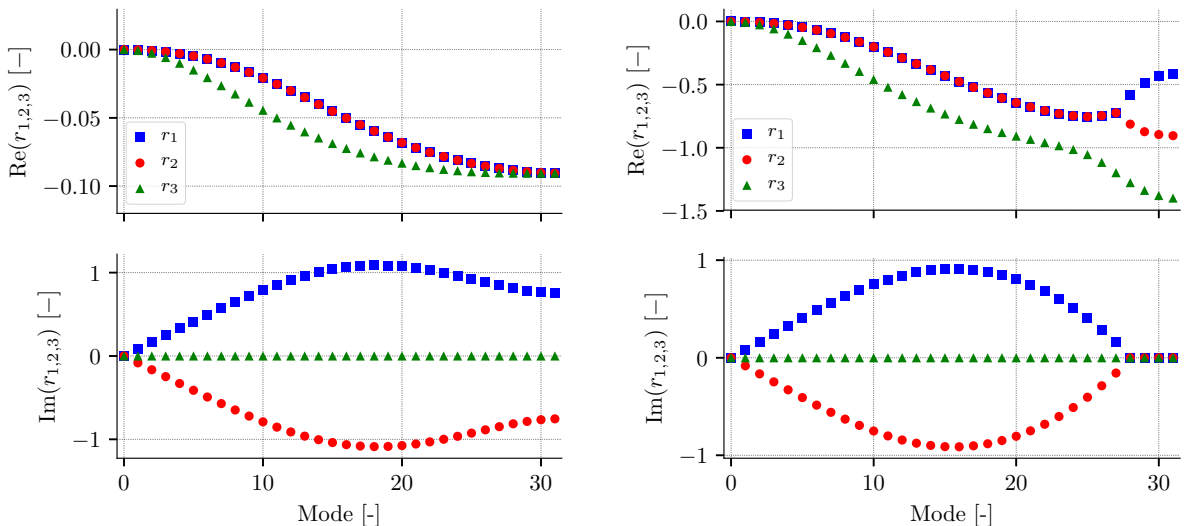


Figure 9: Real (top) and imaginary (bottom) parts of the roots of Q for $\alpha = 0.2$ (left) and 2 (right). Other parameters are $p_{bg}=1$ and $\tilde{\Delta}x=0.143$, $M=3$, $N=63$, $\xi = \alpha/4$ and the quintic kernel was used.

Figure 10 shows the roots of Q for the same parameters as in Fig. 9 except that background pressure is set to zero. It is observed that the angular frequency decreases to zero at higher modes, and that the aperiodic mode starts at lower modes. As mentioned earlier, the continuous mode is not damped ($r_3=0$), for any values of α . Therefore to fully benefit of the advantage of δ -SPH, it is demonstrated here that a strictly positive background pressure is mandatory. However, for a large viscosity (Fig. 10 right), the damping of the aperiodic mode is larger than when the background pressure is positive. This means that high frequency perturbations are faster damped without background pressure, which could be an advantage.

In the present case where $p_{bg}=0$, the value of ξ is not limited by α , as mentioned by Antuono et al. [17], as it appears as a regular viscosity coefficient in the expression of Q (Eq. 67). In this context, Antuono et al. [28] studied the stability of the δ -SPH method when the background pressure is equal to zero. They applied a 1D linear stability analysis with a modified diffusive term in the density equation (ψ_{ab} in Eq. 62a) which is also valid on an incomplete sphere of influence. For a given α , they provided a range of ξ to avoid the aperiodic regime. However, they did not mention the undamped continuous mode. Applying the same type

of analysis with the diffusion operator presented in Eq. 62a leads to the condition on the diffusion constants ξ and α :

$$\frac{\alpha}{2} + \frac{\phi_i}{\Delta x \lambda_i'''} \leq \xi \leq \frac{\alpha}{2} - \frac{\phi_i}{\Delta x \lambda_i'''} \quad (68)$$

which is similar to the one derived by Antuono et al. [28], in the sense that the limiting value depends on $\phi_i/\Delta x \lambda_i'''$ which is related to the maximum resolved wavenumber. Finally, even though the temporal

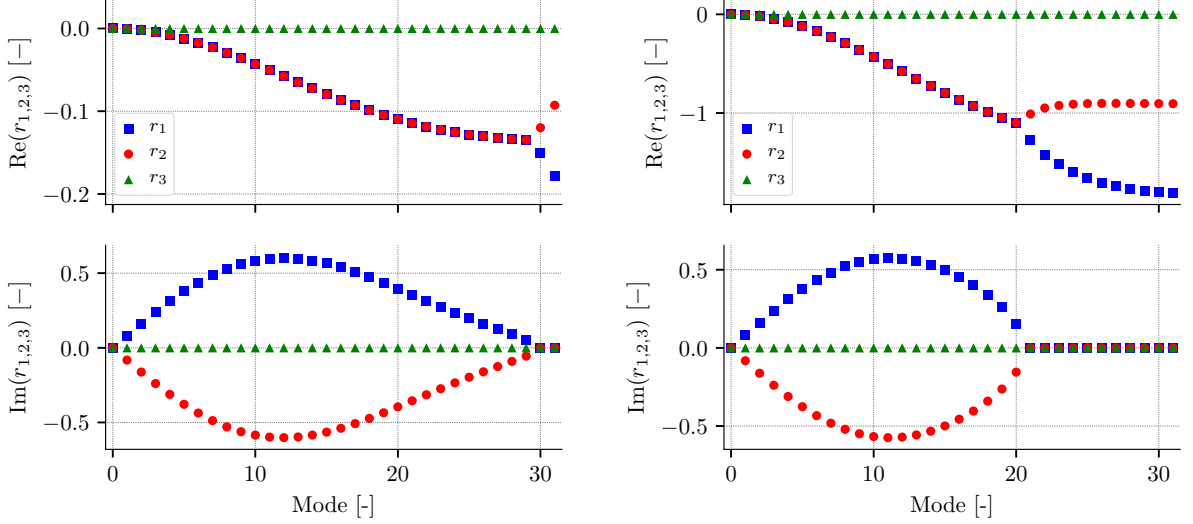


Figure 10: Real (top) and imaginary (bottom) parts of the roots r_1 , r_2 , r_3 of Q for $\alpha = 0.2$ (left) and 2 (right). Other parameters are $p_{bg}=0$ and $\Delta x=0.143$, $M=3$, $N=63$, $\xi = \alpha/4$ and the quintic kernel was used.

solution of the linearized δ -SPH cannot be expressed as an analytical function, Eqs. 66 and 67 are validated in Appendix B.

5. Application of LSA to the Transport Velocity Formulation (TV-SPH)

The Transport-Velocity Formulation of SPH (referred to as TV-SPH in the following) was developed by Adami et al. [19]. The basic idea is to (i) advect particles at a modified transport velocity \tilde{u} that reduces the particle disorder, and (ii) to compute the physical source terms from the original fluid velocity u . The lower particle disorder increases the accuracy of the operators compared to traditional methods. This approach is based on the assumption of incompressible flow even though it is applied to WCSPH. The set of equations is, in 1D:

$$\left\{ \begin{array}{l} \rho_a = m_a \sum_b W_{ab} \quad (69a) \\ \frac{d\tilde{u}_a}{dt} = \frac{1}{m_a} \sum_b (V_a^2 + V_b^2) \left[-\tilde{p}_{ab} W'_{ab} + \frac{1}{2} (T_a + T_b) W'_{ab} + \tilde{\mu}_{ab} \frac{u_{ab}}{x_{ab}} W'_{ab} \right] \quad (69b) \\ p_a = c^2 (\rho_a - \bar{\rho}) \quad (69c) \\ \frac{d\tilde{u}_a}{dt} = \frac{d\tilde{u}_a}{dt} - \frac{p_{back}}{m_a} \sum_b (V_a^2 + V_b^2) W'_{ab} \quad (69d) \\ \frac{dx_a}{dt} = \tilde{u}_a \quad (69e) \end{array} \right.$$

where \tilde{d}/dt is the material derivative of a particle moving with the modified transport velocity and $T = \rho u(\tilde{u} - u)$ is the convection of the particle momentum with the relative velocity ($\tilde{u} - u$). The dynamic viscosity and pressure are expressed with an inter-particle approach as $\tilde{\mu}_{ab} = 2\mu_a \mu_b / (\mu_a + \mu_b)$ and $\tilde{p}_{ab} = (\rho_b p_a + \rho_a p_b) / (\rho_a + \rho_b)$, respectively. It is important to notice that even though \tilde{d}/dt and d/dt are two material derivatives with different advection velocities for the Eulerian point of view, they are equivalent to $\partial/\partial t$ in the Lagrangian framework [12]. In Eqs. 69, the two independent variables are u_a and x_a .

It is assumed that the viscosity is homogenous, *i.e.* $\tilde{\mu}_{ab} = \mu$. The intermediate quantities are linearized to the first-order as:

$$\begin{cases} V_a^2 \approx \bar{V}^2 \left(1 - 2 \frac{\delta \rho_a}{\bar{\rho}} \right) & (70a) \\ \tilde{p}_{ab} \approx \frac{\bar{\rho}_b \delta p_a + \bar{\rho}_a \delta p_b}{\bar{\rho}_a + \bar{\rho}_b} & (70b) \\ T_a \approx \bar{\rho} \bar{u} \bar{w} + \bar{\rho} \bar{u} \delta w_a + \bar{\rho} \bar{w} \delta u_a + \bar{u} \bar{w} \delta \rho_a & (70c) \end{cases}$$

where the relative velocity is decomposed as $w = \tilde{u} - u = \bar{w} + \delta w$. Due to the quadratic dependency of T_a on u , the mean velocity is considered positive only ($\bar{u} \geq 0$) to apply the linearization. The non-dimensionalization and the projection into the mode basis leads to:

$$\begin{cases} \frac{1}{\Delta x} \frac{dv_i}{dt} = [\bar{u} \bar{w} \lambda'_i - (1 + \bar{u} \bar{w}) \Delta x \lambda_i'^2] y_i + [(\bar{w} - \bar{u}) \lambda'_i + 2\nu \lambda_i'''] v_i + \bar{u} \lambda'_i \frac{dy_i}{dt} & (71a) \\ \frac{d^2 y_i}{dt^2} = \frac{dv_i}{dt} + 2 p_{bg} \Delta x (\Delta x \lambda_i'^2 - \lambda_i'') y_i & (71b) \end{cases}$$

where v_i is the general term of the projection of \underline{U} in the mode basis. Expressing the coordinate y_i in the Laplace domain yields:

$$\begin{aligned} Y_i &= P_1(p) y_{i,0} + P_2(p) y'_{i,0} + P_3(p) v_{i,0} \quad \text{with} & (72a) \\ P_1(p) &= p [p - (\bar{w} \lambda'_i + 2\nu \lambda_i''') \Delta x] / Q(p) & (72b) \\ P_2(p) &= [p - ((\bar{w} - \bar{u}) \lambda'_i + 2\nu \lambda_i''') \Delta x] / Q(p) & (72c) \\ P_3(p) &= [(\bar{w} - \bar{u}) \lambda'_i + 2\nu \lambda_i'''] \Delta x / Q(p) & (72d) \end{aligned}$$

and

$$\begin{aligned} Q(p) &= p^3 + \Delta x (\bar{w} \lambda'_i - 2\nu \lambda_i''') p^2 \\ &\quad - \Delta x [2 \pi_{bg} \varphi_i + \Delta x \lambda_i'^2] p \\ &\quad - 2 \Delta x^2 p_{bg} \varphi_i ((\bar{w} - \bar{u}) \lambda'_i - 2\nu \lambda_i''') \end{aligned} \quad (73)$$

where $\pi_{bg} = p_{bg} - \bar{u} \bar{w} / 2$ and $\varphi_i = \lambda_i'' - \Delta x \lambda_i'^2$. As in δ -SPH, the constant part of $Q(p)$ ensures that $p=0$ is not a root. Therefore, $p_{back} > 0$ is a sufficient condition to ensure damping of any perturbations in the case of viscous flow ($\nu > 0$). The Laplace variable of the physical velocity v is labeled Υ and yields:

$$\begin{aligned} \Upsilon_i &= P_1(p) y_{i,0} + P_2(p) y'_{i,0} + P_3(p) v_{i,0} \quad \text{with} & (74a) \\ P_1(p) &= [p^2 (1 - \bar{u} \Delta x \lambda'_i) + p \Delta x (\Delta x \lambda_i'^2 - \bar{u} \bar{w} \varphi_i) - 2 p_{bg} \Delta x \varphi_i] / Q(p) & (74b) \\ P_2(p) &= [\bar{u} \lambda'_i p + \bar{u} \bar{w} \varphi_i - \lambda_i'^2] \Delta x / Q(p) & (74c) \\ P_3(p) &= [p^2 + \bar{u} \Delta x \lambda'_i p - \Delta x (2 \pi_{bg} \varphi_i - \Delta x \lambda_i'^2)] / Q(p) & (74d) \end{aligned}$$

with $Q(p)$ as defined in Eq. 73. Equations 72, 73 and 74 are validated in Appendix B.

Figure 11 displays the real and imaginary part of the roots of $Q(p)$, for $\nu=0.1$ (left) and $\nu=1$ (right). Other parameters are $p_{bg}=1$, $\Delta x=0.143$, $N=63$, $(\bar{u}, \bar{w})=(0,0)$, and the quintic kernel was used. A continuous solution (r_3) is observed for both values of the viscosity. The damping ratio is significantly larger than the oscillating solutions, for a mode number $\gtrsim 10$. For a high mode numbers, the oscillating solutions show a

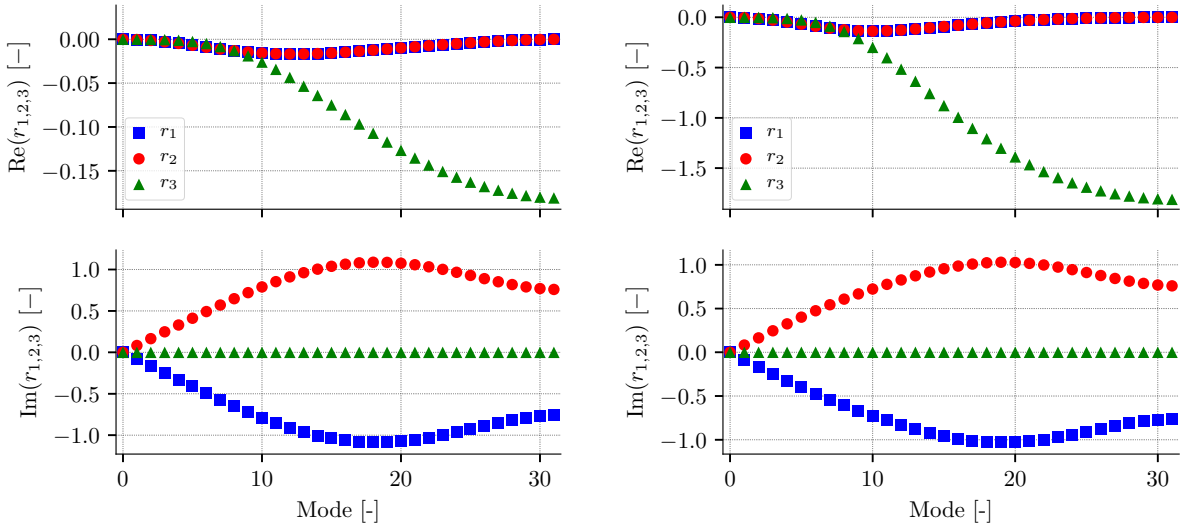


Figure 11: Real (top) and imaginary (bottom) parts of the roots r_1 , r_2 , r_3 of Q for $\nu = 0.1$ (left) and 1 (right). Other parameters are $p_{bg}=1$, $\hat{\Delta}x=0.143$, $N=63$, $(\bar{u}, \bar{w})=(0,0)$ and the quintic kernel.

damping ratio very close to zero, suggesting that high frequency disturbances might be weakly damped. Further investigations, especially concerning the influence of the velocities \bar{u} and \bar{w} are provided when discussing the dispersion curves in the next section.

6. Dispersion curves

In this section, the dispersion curves of the WCSPH methods are investigated as outlined in the previous sections. First, the viscosity is set to zero in order to study the non-damped sound propagation and second, the influence of the viscosity is studied.

In order to quantify the deviation of discrete WCSPH to a continuum, the dispersion curves will be compared to the ones obtained from the linearized Navier-Stokes equations. In this approach, the linearization of mass and momentum conservation leads to:

$$\frac{\partial^2 \delta u}{\partial t^2} - c^2 \frac{\partial^2 \delta u}{\partial x^2} = \nu \frac{\partial^3 \delta u}{\partial x^2 \partial t} \quad (75)$$

Non-dimensionalizing Eq. 75 with the variables h and c , and assuming a solution of the form $\delta u(x, t) = \delta_0 \exp[\hat{i}(\omega t - kx)]$ leads to dispersion relation:

$$\omega^2 - \hat{i}\nu\omega k^2 - k^2 = 0 \quad (76)$$

These solutions will be compared to the SPH solutions in the following. The stability analysis is made in a temporal sense. The location is arbitrarily fixed at $x=0$ and the temporal evolution is investigated. Note that in this case, the stability is obtained for $\text{Im}(\omega) > 0$.

6.1. Propagation in an inviscid medium

6.1.1. Classical WCSPH: sum-SPH

The dispersion curves are obtained by plotting the angular frequency ω_p defined in Eq. 42 versus the non-dimensional wavenumber $\kappa_p = 2\pi\tilde{h}/\lambda_p$. When the viscosity is zero, the angular frequency is given by $\omega_p = \phi_p$. Figure 12 displays the dispersion curve for the quintic kernel (left) and the Wendland kernel

(right), and different p_{bg} . The domain parameters are $N=1000$ and $M=3$. The solid vertical line is related to the diameter of the sphere of influence $D = (2M + 1)\Delta x$ and is labeled κ_D while the dashed vertical line corresponds to the kernel standard deviation \tilde{h} and is located at $\kappa_{\tilde{h}}=2\pi$. The highest resolved wavenumber is $\pi/\Delta x$. The line of equation $y = x$ is the dispersion curve obtained from Eq. 76 and characterizes a non-dispersive medium.

First, it is observed that both kernels have a similar behavior. Hence, the superiority of one kernel compared to the other is not obvious here. Second, due to a low number of neighbors, $M = 3$, the wavenumber $\kappa_{\tilde{h}}$ related to the kernel standard deviation cannot be resolved by the particle lattice.

The ideal non-dispersive behavior is partly retrieved by the SPH scheme for low wavenumbers up to $\approx \kappa_D$. The upper bound of the ideal behavior depends on the background pressure, and the best case is observed for $p_{bg}=1$, independently of the kernel. For $\kappa > \kappa_D$, the angular frequency is not proportional to the wavenumber anymore. Finally, the spurious mode is observed at large wavenumber ($\kappa \approx \pi/\Delta x$) for $p_{bg}=0$.

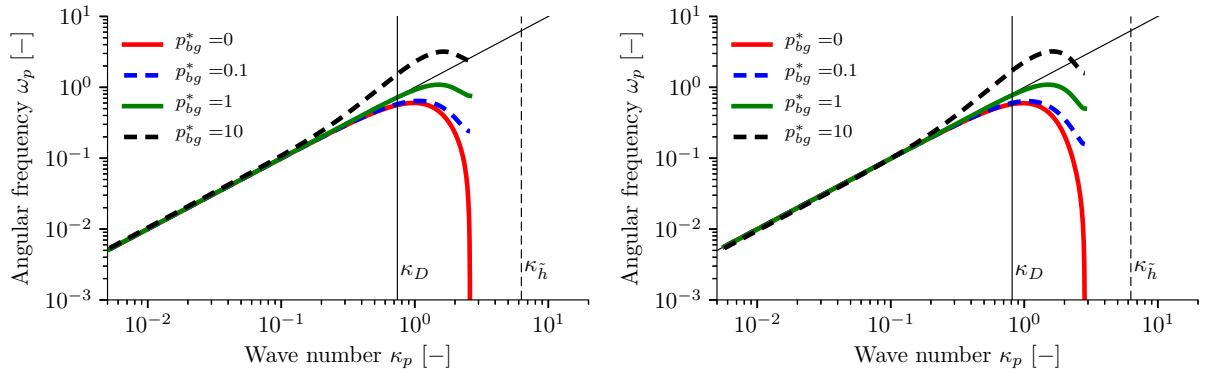


Figure 12: Dispersion curve for $N=1000$ and $\tilde{\Delta}x=0.143$. Left: quintic kernel. Right: Wendland kernel.

From the dispersion relation, it is possible to extract the phase velocity $c_\phi = \omega/\kappa$ and the group velocity $c_g = \partial\omega/\partial\kappa$. They are both shown for the quintic kernel in Fig. 13. On the left, the phase velocity is equal to 1 up to $\approx \kappa_D$, where it depends on p_{bg} , the best case being $p_{bg}=1$ as previously mentioned. Contrary to the phase velocity c_ϕ , the group velocity c_g (Fig. 13, right) becomes negative at high wavenumbers. It is observed that a larger background pressure increases the wavenumber at which c_g becomes negative. Note that for a wavenumber leading to $c_g < 0$, the previous results (*e.g.* Fig. 12) show no instability. Therefore, a negative group velocity does not imply an instability. On the other hand, setting $p_{bg} > 1$ increases the group velocity for $\kappa \lesssim \kappa_D$, meaning that the pressure information propagates at a speed faster than c . As for the phase velocity, the best compromise is found for $p_{bg}=1$.

The dispersion curve for $\tilde{\Delta}x=0.048$ ($M=10$) is shown in Fig. 14 for the quintic kernel (left) and the Wendland kernel (right). The same characteristics with regards to the background pressure are observed. However, in this case due to the larger number of neighbors, the particle lattice can resolve wavelengths smaller than \tilde{h} . The spurious modes when $p_{bg}=0$ occurs several time for the quintic kernel, while it occurs only at κ_{max} for the Wendland kernel. This suggests a better stability of the Wendland kernel with a large number of neighbors when $p_{bg}=0$. The corresponding phase and group velocities are depicted in Fig. 15 for the quintic kernel. The same findings as for $\tilde{\Delta}x=0.143$ are valid. In addition, for $\kappa > \kappa_{\tilde{h}}$, the group velocity is almost zero.

6.1.2. Other methods without viscosity

When the viscosity is set to zero in div-SPH and δ -SPH, the roots of $Q(p)$, labeled as π_i^\pm , are zero and $\pm\phi_i$, and the dispersion curve of these methods is the same as the one obtained from sum-SPH, with an

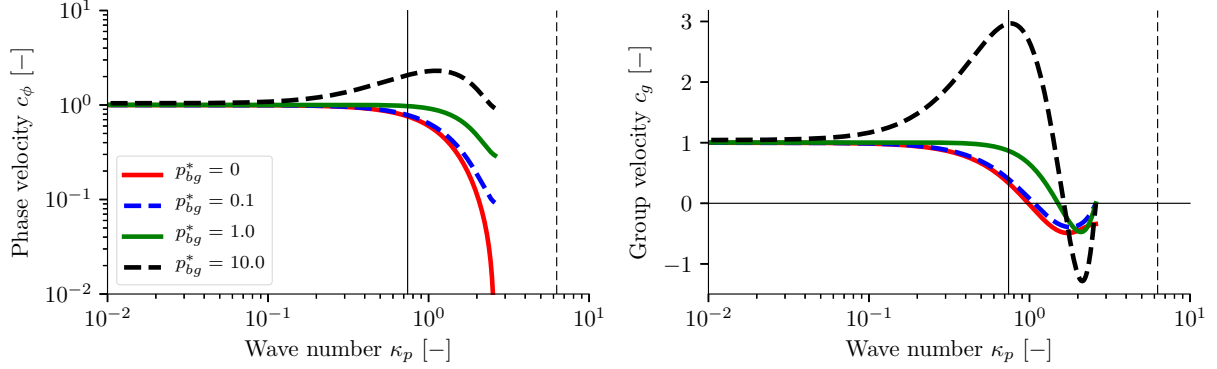


Figure 13: Phase (left) and group (right) velocity for $N=1000$, $\tilde{\Delta}x=0.143$ and the quintic kernel.

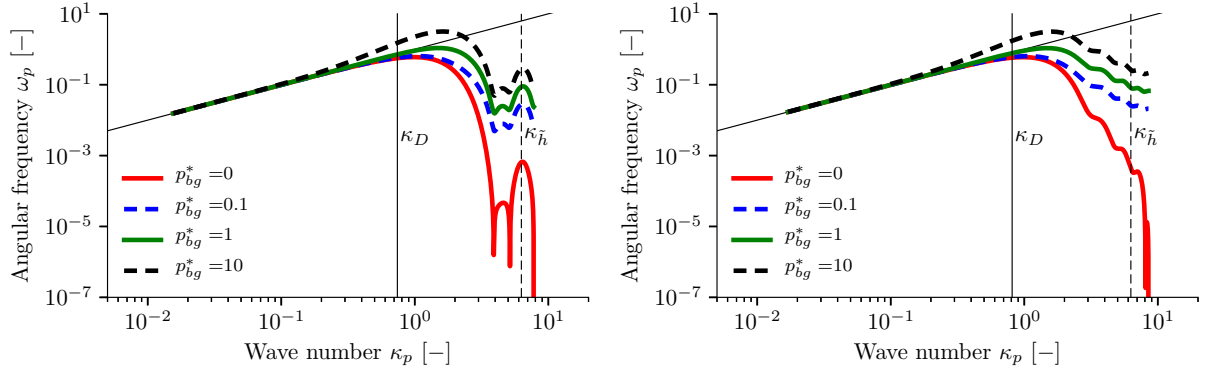


Figure 14: Dispersion curve for $N=1000$ and $\tilde{\Delta}x=0.048$. Left: quintic kernel. Right: Wendland kernel.

additional continuous component. Concerning TV-SPH, it also depends on the mean velocity \bar{u} and the mean velocity difference \bar{w} . When both of them are zero, the roots of $Q(p)$ are also 0 and $\pm\phi_i$, leading to the regular dispersion curve plus a continuous component. However, when $\bar{w}=0$ and $\bar{u} > 0$, the polynomial Q is:

$$Q(p) = p^3 + \phi_i^2 p + 2 \Delta x^2 p_{bg} \phi_i \bar{u} \lambda'_i \quad (77)$$

The roots of Eq. 77 were numerically computed for $(\bar{u}, \bar{w})=(0.05,0)$, $p_{bg}=1$, $N=1000$ and $M=3$. All roots have a real part equal to zero so no damping is found. The imaginary part of the roots of Eq. 77 are depicted in Fig. 16. It is obvious that, in addition to the regular oscillations following the line $y = x$, there are additional oscillations of lower frequency. This means that when both the physical and transport velocity are close (*i.e.* $\bar{w} \approx 0$), a spatial excitation results in a superposition of several frequencies, which can be regarded as a non-linear behavior.

When $\bar{w} \neq 0$ and $\bar{u} > 0$, the polynomial Q is:

$$Q(p) = p^3 + \Delta x \bar{w} \lambda'_i p^2 - \Delta x [2 \pi_{bg} \phi_i + \Delta x \lambda_i'^2] p - 2 \Delta x^2 p_{bg} \phi_i ([\bar{w} - \bar{u}] \lambda'_i) \quad (78)$$

The roots of Eq. 78 were numerically computed for $(\bar{u}, \bar{w})=(0.05,-0.05)$, the other parameters being identical to the previous case. Like in the previous case, all roots have a real part equal to zero, and a additional

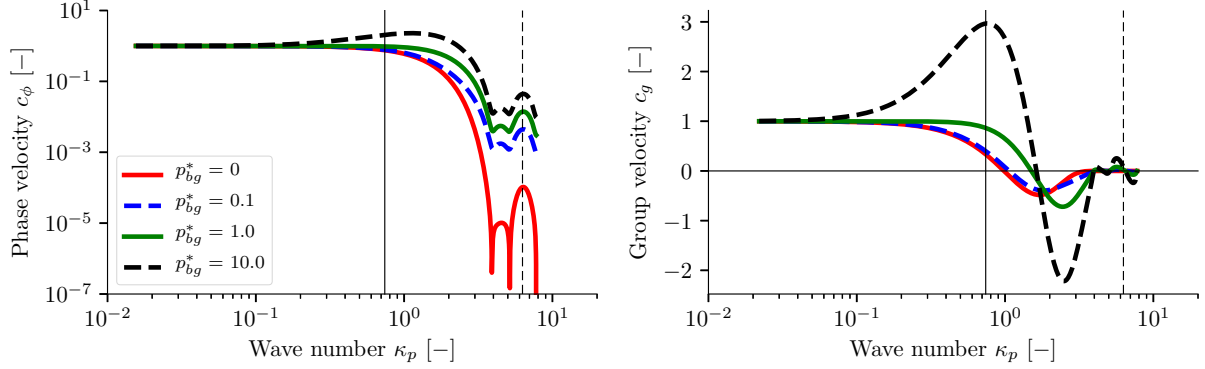


Figure 15: Phase (left) and group (right) velocity for $N=1000$, $\tilde{\Delta}x=0.048$ and the quintic kernel.

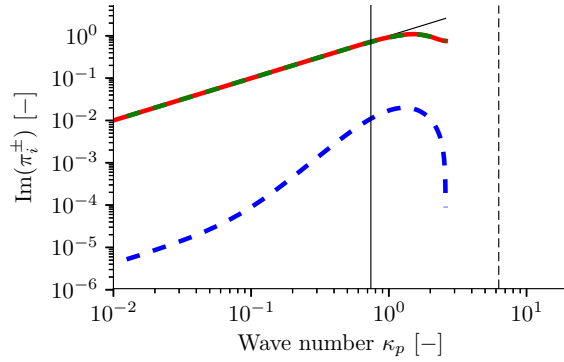


Figure 16: Absolute value of the imaginary part of the roots of Q for $p_{bg}=1$, $\tilde{\Delta}x=0.143$, the quintic kernel and $(\bar{u}, \bar{w})=(0.05, 0)$

mode of lower frequency is also found. The particular case $\bar{u} = \bar{w} \neq 0$ leads to a polynomial Q :

$$Q(p) = p(p^2 + \Delta x \bar{w} \lambda'_i p + \phi_i^2) \quad (79)$$

Although this polynomial is different from the one obtained for $\bar{u} = \bar{w} = 0$, the roots are almost the same and the real part is always zero.

6.2. Effects of viscosity

6.2.1. sum-SPH

Due to the damping ratio in the differential equation of motion, not only the imaginary part of π_i but also its real part is presented and compared to the continuum solution. The solutions of Eq. 42 are presented in Fig. 17 for the quintic kernel, $N=500$, $p_{bg}=0.5$, $\tilde{\Delta}x=0.143$ (left) and $\tilde{\Delta}x=0.048$ (right), and compared to the continuum solution, labeled CON in figures. For $\tilde{\Delta}x=0.143$, $p_{bg}=0.5$ leads to a good prediction in terms of damping ratio, but the best agreement for angular frequency is found for $p_{bg}=1$. For $\tilde{\Delta}x=0.048$, a large viscosity ($\nu=1$) shows a good agreement with the continuum solutions, whereas with $\nu=0.1$, the sum-SPH method predicts damping without oscillations starting at $\kappa \approx \kappa_{\tilde{h}}$ although the continuum solution shows damped oscillations. The risk of instability is also observed for $\tilde{\Delta}x=0.048$ at $\kappa \approx \kappa_{\tilde{h}}$ where the spurious mode ($\omega_i=0$) shows a very low damping ratio. Finally, it is to be mentioned that the prefactor of the Laplacian operator in Eq. 6b was set to 2 and not as proposed by Maciá et al. [29]. According to their derivation, the

proper pre-factor is $2(n_d + 2)$ where n_d is the number of dimension, which would be equal to 6 here. In this case, the damping ratio of sum-SPH would be overestimated by a factor of 3.

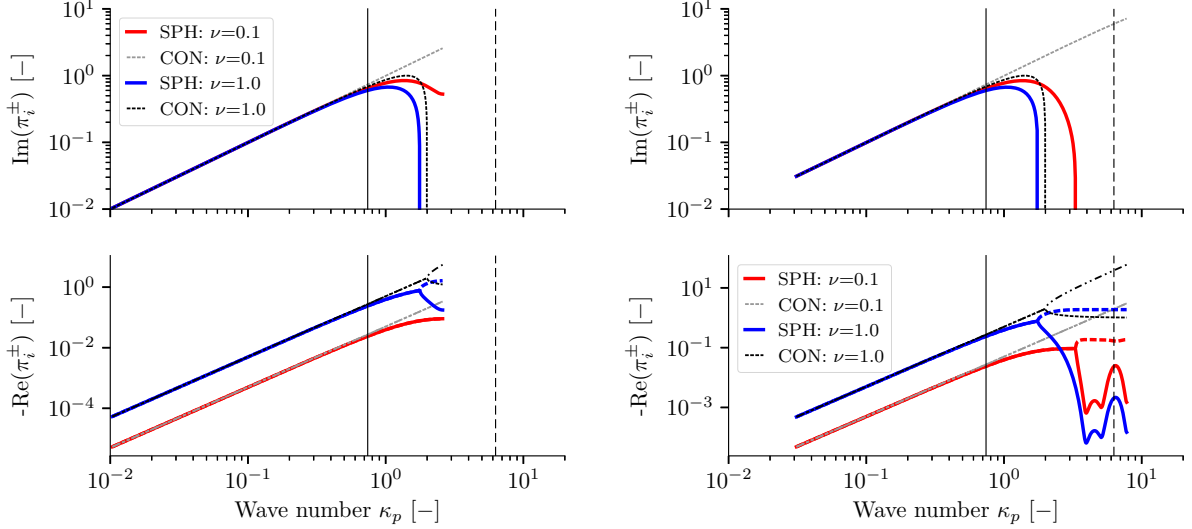


Figure 17: Imaginary and real part of angular frequency π_i^\pm versus the wavenumber κ for the quintic kernel and $p_{bg}=0.5$, superimposed with the continuum solution. For SPH, solid and dashed lines represent π_i^+ and π_i^- , respectively, whereas they are represented by dashed and dot-dashed lines for the continuum solution. Left: $\tilde{\Delta}x=0.143$. Right: $\tilde{\Delta}x=0.048$.

The same investigation with the Wendland kernel is shown in Fig. 18. When $\tilde{\Delta}x=0.143$, the Wendland kernel is very similar to the quintic kernel. When $\tilde{\Delta}x=0.048$, at high wavenumber ($\kappa \approx \kappa_{\tilde{h}}$), the Wendland kernel shows a monotonic decrease and a larger damping ratio than for the quintic kernel. For both kernels, the best value of p_{bg} depends on the quantity to match. For a better prediction of the sound speed p_{bg} should be one, whereas the best agreement for the damping is found for $p_{bg} \approx 0.5$.

6.2.2. δ -SPH

The dispersion curve of δ -SPH method is presented in this subsection. As the poles of the transfer function cannot be analytically expressed in a compact form, they are computed numerically. Figure 19 shows the imaginary and real part of the solution for the quintic kernel, $p_{bg} = 0.5$, $\Delta x=0.86$ and $\xi = \alpha/4$. Different values of the viscosity $\alpha=0.2$ (left) and $\alpha=2$ (right) were investigated. The imaginary part of the damped continuous mode identified in Section 4 cannot be shown in a log-log plot because it is equal to zero. Its real part, *i.e.* its damping ratio, is approximately two times larger than the damping ratio of the oscillating modes. Hence, the unphysical continuous mode is damped faster than physical oscillations. As in sum-SPH, the best agreement with the continuum for the sound speed is $p_{bg} = 1$ whereas it is $p_{bg} \approx 0.5$ for the damping coefficient. Investigations with the Wendland kernel showed very little difference to the quintic kernel. With $\Delta x=0.29$, the findings of sum-SPH apply also to δ -SPH.

6.2.3. TV-SPH

The poles of the transfer function (Eq. 73) are computed numerically. They are depicted in Fig. 20 for the quintic kernel, $p_{bg}=0.5$, $\Delta x=0.86$ and $(\bar{u}, \bar{w})=(0,0)$. The artificial continuous mode is still observed (not depicted in the log-log plot of the imaginary part) but it is damped. The damping ratio is significantly lower than that of the continuum solution up to κ_D , independently of the viscosity. For $\nu=1$ (Fig. 20 right), large wavenumbers show weakly damped oscillations whereas for the continuum solution a damped aperiodic regime is predicted. This phenomenon is always observed for other values of (\bar{u}, \bar{w}) . It was also observed but not depicted here, that a lower background pressure decreases the damping ratio of the non-physical

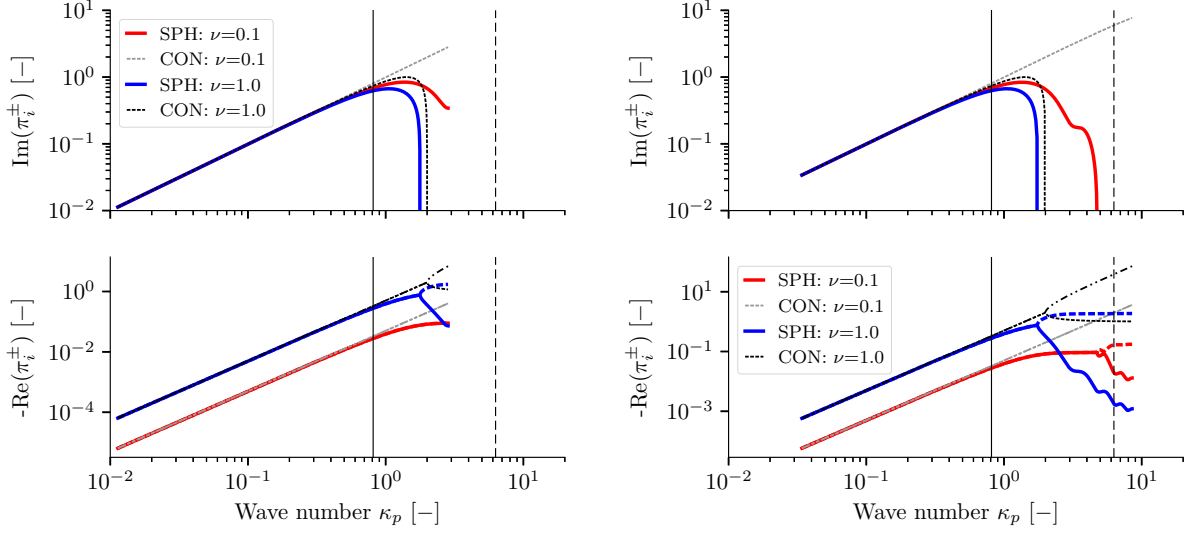


Figure 18: Imaginary and real part of angular frequency π_i^\pm versus the wavenumber κ for the Wendland kernel and $p_{bg} = 0.5$, superimposed with the continuum solution. $\Delta x=0.143$ (left) and $\Delta x=0.048$ (right). For SPH, solid and dashed lines represent π_i^+ and π_i^- , respectively, whereas they are represented by dashed and dot-dashed lines for the continuum solution.

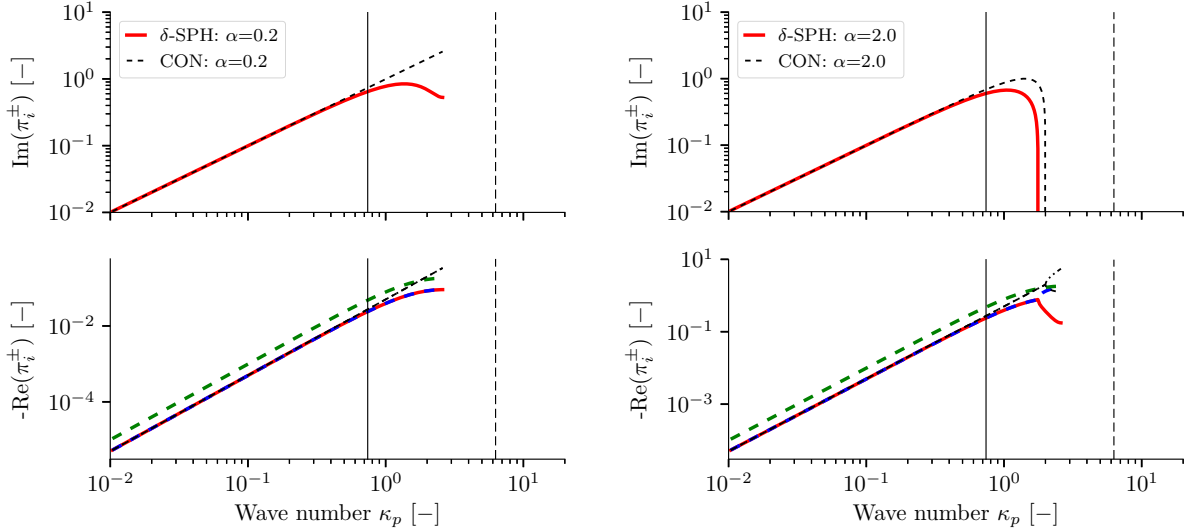


Figure 19: Imaginary and real part of angular frequency π_i^\pm versus the wavenumber κ for the quintic kernel, $p_{bg} = 0.5$ and $\Delta x=0.143$, superimposed with the continuum solution. Left: $\alpha=0.2$. Right: $\alpha=2$. For SPH, solid and dashed lines represent π_i^+ and π_i^- , respectively, whereas they are represented by dashed and dot-dashed lines for the continuum solution. The continuous mode of δ -SPH is represented by a green dashed line.

mode and increases the damping ratio of the physical oscillations at high wavenumber, and *vice versa*. This suggests that there exist an optimal background pressure for the prediction of acoustic waves with the TV-SPH method.

Solutions for $(\bar{u}, \bar{w})=(0,0.1)$ and $\nu=0.1$ are depicted in Fig. 21 (left). In this case, the non-physical continuous mode is turned into a low-frequency π mode and shows the same damping characteristics as in

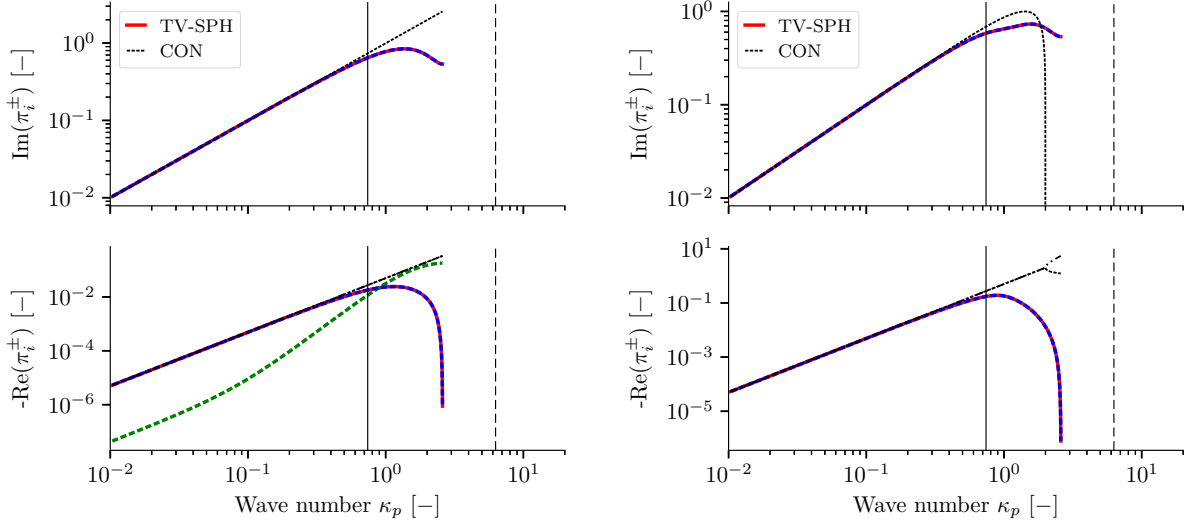


Figure 20: Imaginary and real part of angular frequency π_i^\pm versus the wavenumber κ for the quintic kernel, $p_{bg} = 0.5$ and $\tilde{\Delta}x=0.143$, superimposed with the continuum solution. Particular parameters are $(\bar{u}, \bar{w})=(0,0)$. Left: $\nu=0.1$. Right: $\nu=1$. For SPH, solid and dashed lines represent π_i^+ and π_i^- , respectively, while the continuous mode is represented by a green dashed line. For the continuum solution, they are represented by dashed and dot-dashed lines.

Fig. 20. The result of a positive fluid velocity $(\bar{u}, \bar{w})=(0.05, 0.1)$ is shown in Fig. 21 (right) and highlights the presence of instabilities at large wavenumber. They are depicted by cross symbols in Fig. 21 and represent $+\text{Re}(\pi_i)$ instead of $-\text{Re}(\pi_i)$. This instability is illustrated in Appendix B.

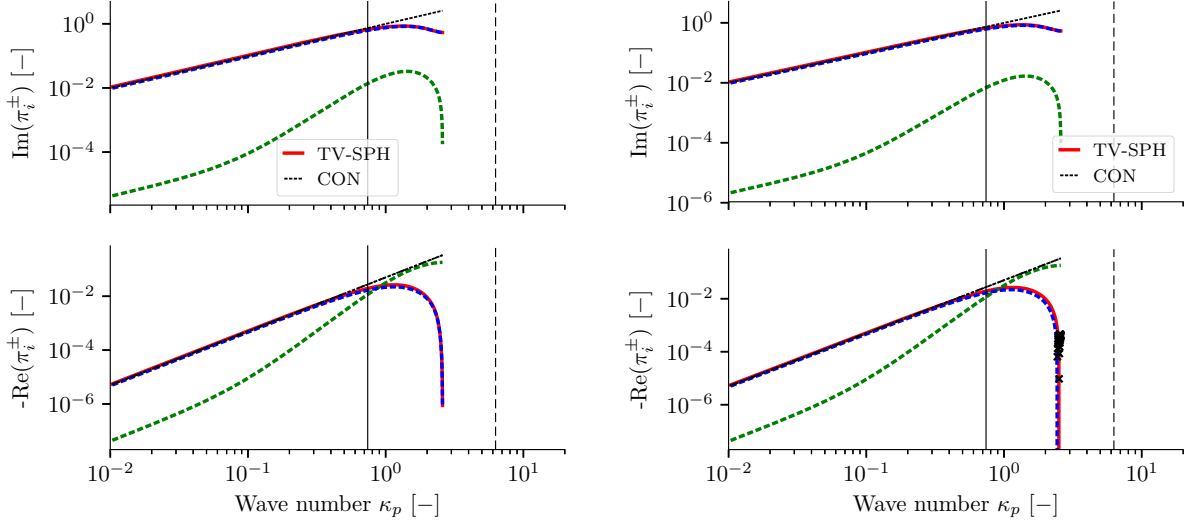


Figure 21: Imaginary and real part of angular frequency π_i^\pm versus the wavenumber κ for the quintic kernel, $p_{bg} = 0.5$, $\tilde{\Delta}x=0.143$ and $\nu=0.1$, superimposed with the continuum solution. Left: $(\bar{u}, \bar{w})=(0,0.1)$. Right: $(\bar{u}, \bar{w})=(0.05, 0.1)$. For SPH, solid and dashed lines represent π_i^+ and π_i^- , respectively, while the continuous mode is represented by a green dashed line. For the continuum solution, they are represented by dashed and dot-dashed lines.

7. Illustration of the spurious mode with a large number of neighbors

This section illustrates the difference between the quintic and the Wendland kernel if a large number of neighbor particles are present ($M=9 \Leftrightarrow \Delta x=0.32$) with $p_{bg}=1$ and $\nu=0$. Special emphasis is put on the spurious mode as observed in Fig. 5. The number of particle N is 60. The dispersion curves c_ϕ and c_g are plotted for the quintic and the Wendland kernel in Fig. 22 with several modes that represent different states. Note that in this figure, the normalizing length scale is D in order to display the modes at the same position independently from the kernel. Mode 6 corresponds to a phase velocity close to the continuum solution and a group velocity ≈ 0 , mode 9 shows a negative group velocity of magnitude ≈ 1 . Mode 20 and 30 have a phase velocity $\ll 1$. In particular, mode 20 is the spurious mode for the quintic kernel. Mode 30 shows a group velocity ≈ 0 .

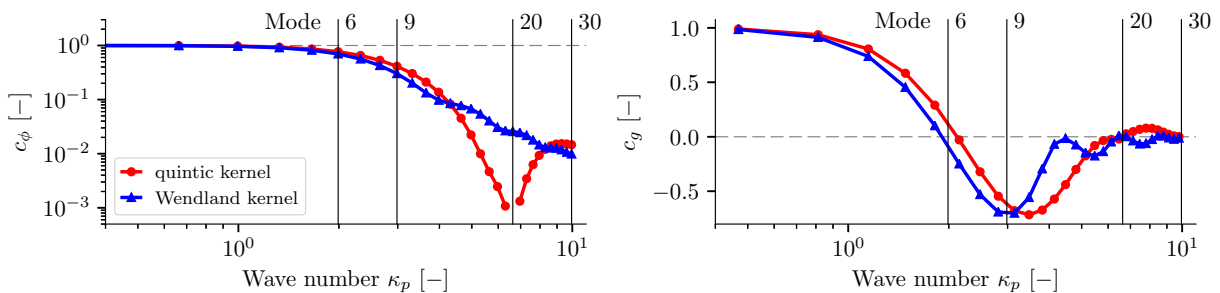


Figure 22: Dispersion curve for $(N,M)=(60,9)$. Left: Phase velocity. Right: Group velocity. The vertical lines correspond to mode 6, 9, 20 and 30

In order to compare the LSA results with a real simulation, 1D sum-SPH simulations were run. The same numbers (N,M) were used and $p_{bg}=1$ and $\nu=0$ were set. The rest of the numerical parameter are the same as those presented in Appendix B. An initial excitation velocity of 1% of the speed of sound was applied, and the simulations were run for a long non-dimensional time. The focus is put on the long time instability with a large deviation from the equilibrium state. Hence, the temporal solution of the linearized perturbation may not apply.

In Fig. 23 to 25 the normalized position of each particle is plotted versus non-dimensional time, for the quintic kernel (left figures) and the Wendland kernel (right figures).

With the mode 6, both kernels show a stable behavior even though the group velocity is almost zero. Therefore, the trajectories are not shown. At mode 9 (Fig. 23), the quintic kernel shows long time instability whereas the Wendland kernel is stable. At mode 20 (Fig. 24), the spurious mode of the quintic kernel is visible with all particles moving at their initial velocity, as predicted by Eq. 46, until $t \approx 1600$. The trajectories show that particles are crossing each other, in such an orchestrated way so that neither the pressure gradient nor the background pressure can counteract this motion. This is striking because even though the temporal solutions of the linearized equations (Eq. 46) may not apply due to the large deviation from the initial position, the behavior highlighted in Fig. 24 still corresponds to the linearized solution. As observed in Fig. 5, the Wendland kernel is not subject to the spurious mode, and provides a stable solution. For mode 30 (Fig. 25), both kernels shows regular oscillations until $t \approx 500$. For $t \gtrsim 500$, the quintic kernel shows an unstable behavior with particle trajectories crossing each other whereas the Wendland kernel shows stable oscillations. These plots underline the more stable behavior of the Wendland kernel in case of large initial deviation from equilibrium. It also shows one more time that a negative group velocity does necessary lead to instability.

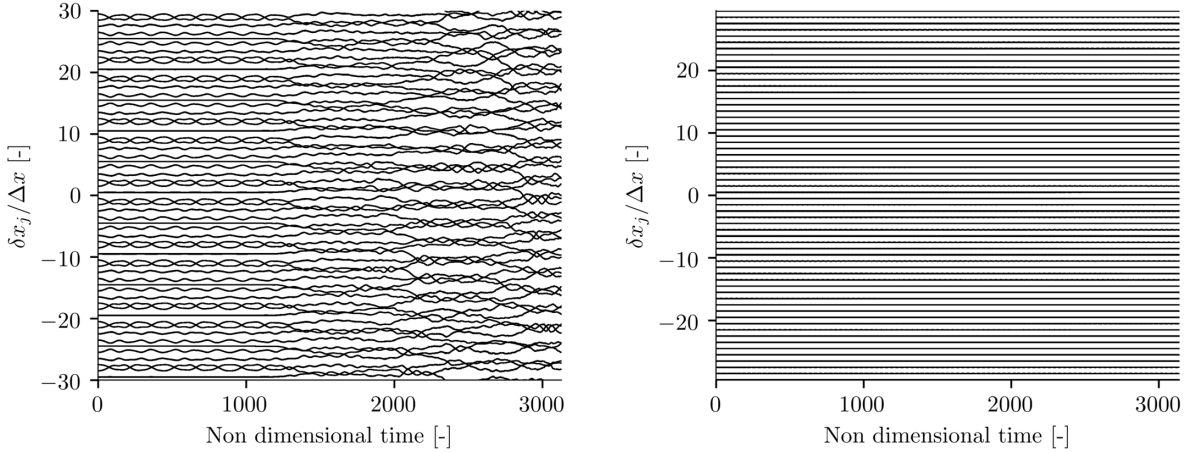


Figure 23: Mode 9: Graph of the particles position for $N=60$. Left: quintic kernel. Right: Wendland Kernel.

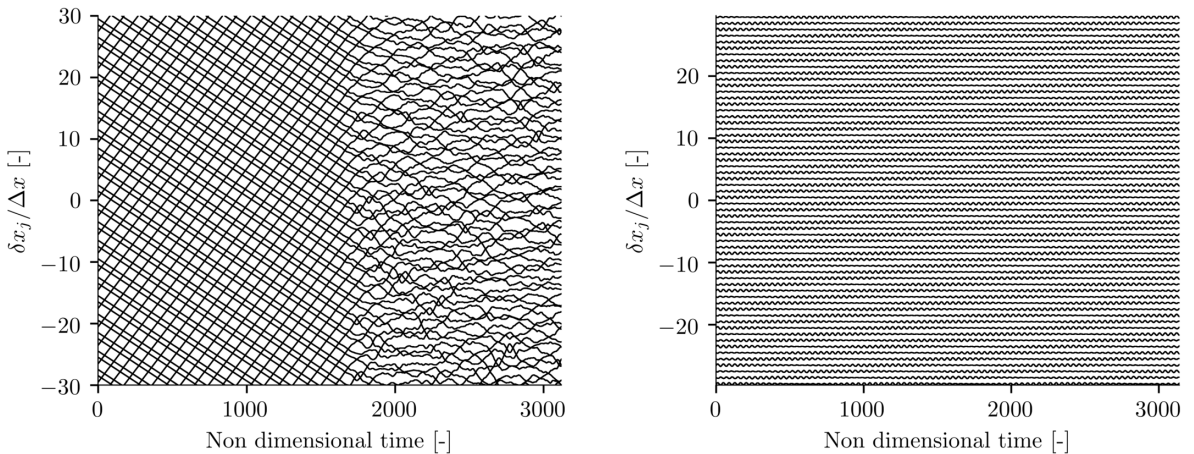


Figure 24: Mode 20: Graph of the particles position for $N=60$. Left: quintic kernel. Right: Wendland Kernel.

8. Conclusion

In this study, a new method for studying the linear stability of the SPH method was presented and applied to different WCSPH methods on a 1D periodic domain. This method does not make any assumptions on the type of the perturbations and allows to resolve the transient temporal evolution of the perturbations. The equations of perturbations are written as a matrix ordinary differential equation in time where the coefficients are circulant matrices. The different SPH operators such as the gradient and the Laplacian can be represented by circulant matrices. Due to the properties of circulant matrices, the diagonalization of the system is equivalent to applying a spatial discrete Fourier transform. It is shown that the stability of the system depends on the discrete Fourier transform of the first and second derivative of the kernel, and the damping is determined by the discrete Fourier transform of $W'(x)/x$.

Four different WCSPH methods, namely sum-SPH, div-SPH, δ -SPH and TV-SPH, were studied with the help of circulant matrices. All the derivations were validated with numerical simulations. It was also observed that some results obtained with linear approximations can hold even with large non-linear perturbations. When the background pressure is positive and of the order of magnitude of ρc^2 , no tensile nor

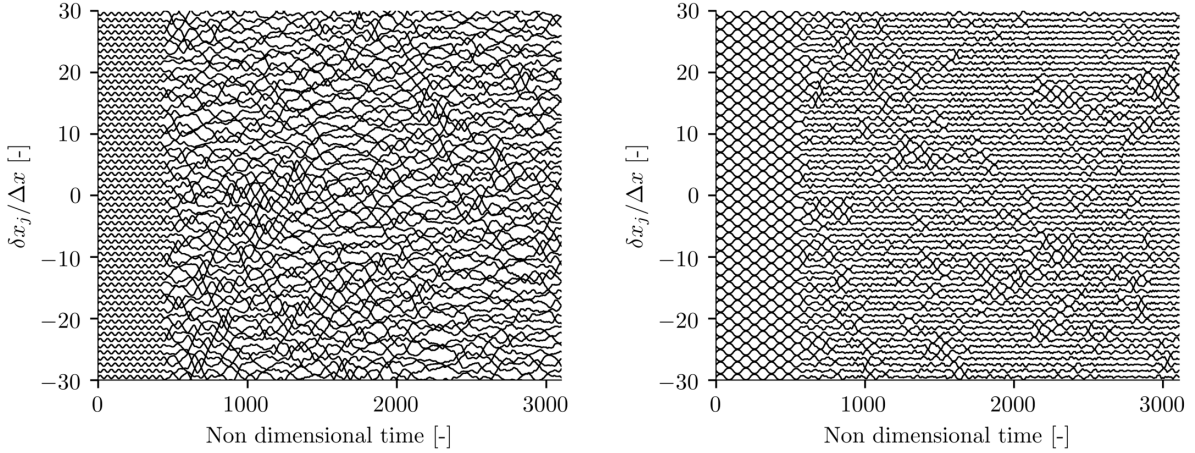


Figure 25: Mode 30: Graph of the particles position for $N=60$. Left: quintic kernel. Right: Wendland Kernel.

pairing instability was found. However, it was found for the first time with sum-SPH and div-SPH that when the background pressure exceeds a critical value, an instability arises. This critical background pressure was not investigated with δ -SPH and TV-SPH.

The resolution of the transient state showed that with div-SPH, a perturbation of position and/or density would remain unaffected, which might explain the necessity to renormalize the density with this method. Therefore, it is advised to avoid the use of div-SPH and use δ -SPH instead. Also, the TV-SPH method showed a slowly growing instability under particular conditions.

The dispersion curve of the four investigated methods was plotted for inviscid and viscous flows. It was observed that the sum-SPH method provides the best agreement to the continuum solution. The δ -SPH method also provides a good prediction, because, due to its additional diffusion terms, the artificial continuous mode inherited from div-SPH is damped faster than physical oscillations. For these two methods, it was also found that the background pressure must be set to ρc^2 to predict the correct sound speed over the largest range of wavelength. However, when the viscous effects are taken into account, the best damping ratio was found for a background pressure $\approx \rho c^2/2$. With a large number of neighbors, the Wendland kernel showed a more stable behavior featuring less spurious modes than the quintic kernel.

It was also demonstrated for the first time that the background pressure in combination with the uncorrected gradient operator counteracts any perturbations of equilibrium. In other words, particles will rearrange in a manner to counteract the particle disorder. Also, the present results is different from those of Fulk [7] and Sweigle et al. [8] who found that the stability depends on the second derivative of the kernel only, whereas our study showed that the stability depends on the first and second derivatives of the kernel.

The fact that no tensile nor pairing instabilities were found with sum-SPH and div-SPH can be explained by the fact that the base mean flow is incompressible. The next steps of this study are (i) to investigate the influence of the integration scheme, as done by Violeau and Leroy [15], and (ii) to apply the circulant matrix decomposition on a 2D configuration, in order to study the effect of a transverse instability.

9. Acknowledgement

The Authors like to thank the Helmholtz Association of German Research Centres (HGF) for funding (Grant No. 34.14.02).

10. Nomenclature

Roman letter	Unit	Description
a	[-]	Particle of interest
b	[-]	Neighbor particle
c	[m/s]	Speed of sound
f	[-]	Temporal function of the initial position
g	[-]	Temporal function of the initial velocity
h	[-]	Temporal function of the initial density
h	[m]	Smoothing length
\tilde{h}	[m]	Standard deviation of the kernel
i, j	[-]	Indices
\tilde{i}	[-]	Imaginary number
k	[1/m]	Wave vector
m	[kg]	Mass
p	[Pa]	Pressure
p	[-]	Laplace variable
r	[-]	Roots of a polynomial
u	[m/s]	Velocity
w	[m/s]	Relative velocity in TV-SPH
x	[m]	Position
y	[-]	Position perturbation in the modal space
y_i	[-]	General term of the position perturbation vector
\underline{A}'	[1/m ²]	Circulant matrix related compressibility
\underline{A}''	[1/m ³]	Circulant matrix related to background pressure
\underline{A}'''	[1/m ³]	Circulant matrix related to viscosity
\underline{M}	[-]	Number of neighbors on one side
N	[-]	Total number of particles
\underline{P}	[-]	Change-of-basis matrix
\underline{P}	[Pa]	Vector of pressure perturbation
$P(p)$	[-]	Numerator of a rational function
$Q(p)$	[-]	Denominator of a rational function
\underline{R}	[kg/m ³]	Vector of density perturbation
V	[m ³]	Volume, length in 1D
W	[1/m]	Kernel
\underline{X}	[m]	Vector of position perturbation
\underline{Y}	[-]	Vector of position perturbation in the modal space
Y_i	[-]	Position perturbation in the Laplace domain
Z_i	[-]	Density perturbation in the Laplace domain
Greek letter	Unit	Description
γ	[-]	Polytropic ratio
δ	[-]	Perturbation
κ	[-]	Wave number
λ_p	[-]	Wave length
λ'	[1/m ²]	Eigenvalue of \underline{A}'
λ''	[1/m ³]	Eigenvalue of \underline{A}''
λ'''	[1/m ³]	Eigenvalue of \underline{A}'''
ν	[m ² /s]	Kinematic viscosity
ρ	[kg/m ³]	Density
ϕ_i	[-]	Undamped angular frequency
$\psi_{1,i}$	[-]	First term of ϕ_i^2
$\psi_{2,i}$	[-]	Second term of ϕ_i^2
ω	[-]	Angular frequency
Δ_i	[-]	Discriminant
Δt	[m]	Time step

Δx	[m]	Particle spacing
$\underline{\underline{\Delta}}'$	[-]	Diagonal matrix equivalent to $\underline{\underline{A}}'$
$\underline{\underline{\Delta}}''$	[-]	Diagonal matrix equivalent to $\underline{\underline{A}}''$
$\underline{\underline{\Delta}}'''$	[-]	Diagonal matrix equivalent to $\underline{\underline{A}}'''$
Υ_i	[-]	Velocity perturbation in the Laplace domain

11. References

References

- [1] R. Gingold, J. J. Monaghan, Smoothed particle hydrodynamics-theory and application to non-spherical stars, *Mon. Not. R. Astron. Soc.* 181 (1977) 375–389.
- [2] L. Lucy, A numerical approach to the testing of fission hypothesis, *The Astronomical Journal* 82 (12) (1977) 1013 – 1024.
- [3] J. Monaghan, Smoothed Particle Hydrodynamics, *Annual Review of Astronomy and Astrophysics* 30 (1992) 543 – 574.
- [4] J. J. Monaghan, Simulating free surface flows with SPH, *J. Comput. Phys.* 110 (2) (1994) 399–406.
- [5] M. Liu, G. Liu, Smoothed Particle Hydrodynamics (SPH): an Overview and Recent Developments, *Archives of Computational Methods in Engineering* 17 (2010) 25 – 76.
- [6] A. Colagrossi, B. Bouscasse, M. Antuono, S. Marrone, Particle packing algorithm for SPH schemes, *Computer Physics Communications* 183 (8) (2012) 1641 – 1653, ISSN 0010-4655, doi:<http://dx.doi.org/10.1016/j.cpc.2012.02.032>, URL <http://www.sciencedirect.com/science/article/pii/S0010465512001051>.
- [7] D. A. Fulk, A numerical analysis of smoothed particle hydrodynamics, Tech. Rep., Air Force Institute of Technology, 1994.
- [8] J. Swegle, D. Hicks, S. Attaway, Smoothed particle hydrodynamics stability analysis, *Journal of computational physics* 116 (1) (1995) 123–134.
- [9] D. S. Balsara, Von Neumann stability analysis of smoothed particle hydrodynamics—Suggestions for optimal algorithms, *Journal of Computational Physics* 121 (2) (1995) 357–372.
- [10] J. P. Morris, A study of the stability properties of smooth particle hydrodynamics, *Publications of the Astronomical Society of Australia* 13 (1) (1996) 97–102.
- [11] F. A. Rasio, Particle methods in astrophysical fluid dynamics, *Progress of Theoretical Physics Supplement* 138 (2000) 609–621.
- [12] T. Belytschko, Y. Guo, W. K. Liu, S. P. Xiao, A unified stability analysis of meshless particle methods, *International Journal for Numerical Methods in Engineering* 48 (9) (2000) 1359–1400.
- [13] S. Børve, M. Omang, J. Trulsen, Two-dimensional MHD smoothed particle hydrodynamics stability analysis, *The Astrophysical Journal Supplement Series* 153 (2) (2004) 447.
- [14] W. Dehnen, H. Aly, Improving convergence in smoothed particle hydrodynamics simulations without pairing instability, *Monthly Notices of the Royal Astronomical Society* 425 (2) (2012) 1068–1082, ISSN 1365-2966, doi:[10.1111/j.1365-2966.2012.21439.x](https://doi.org/10.1111/j.1365-2966.2012.21439.x), URL <http://dx.doi.org/10.1111/j.1365-2966.2012.21439.x>.
- [15] D. Violeau, A. Leroy, On the maximum time step in weakly compressible SPH, *Journal of Computational Physics* 256 (2014) 388–415.
- [16] J. J. Monaghan, Smoothed particle hydrodynamics, *Reports on Progress in Physics* 68 (2005) 1703 – 1759.
- [17] M. Antuono, A. Colagrossi, S. Marrone, D. Molteni, Free-surface flows solved by means of SPH schemes with numerical diffusive terms, *Computer Physics Communications* 181 (3) (2010) 532–549.
- [18] S. Marrone, A. Colagrossi, M. Antuono, G. Colicchio, G. Graziani, An accurate SPH modeling of viscous flows around bodies at low and moderate Reynolds numbers, *Journal of Computational Physics* 245 (2013) 456–475.
- [19] S. Adami, X. Hu, N. A. Adams, A transport-velocity formulation for smoothed particle hydrodynamics, *Journal of Computational Physics* 241 (2013) 292–307.
- [20] N. J. Quinlan, M. Basa, M. Lastiwka, Truncation error in mesh-free particle methods, *International Journal for Numerical Methods in Engineering* 66 (13) (2006) 2064–2085.
- [21] J. Morris, P. Fox, Y. Zhu, Modeling Low Reynolds Number Incompressible Flows Using SPH, *Journal of Computational Physics* 136 (1997) 214 – 226.
- [22] H. Wendland, Piecewise polynomial, positive definite and compactly supported radial functions of minimal degree, *Advances in Computational Mathematics* 4 (1995) 389 – 396.
- [23] P. Cleary, J. J. Monaghan, Conduction Modelling Using Smoothed Particle Hydrodynamics, *Journal of Computational Physics* 148 (1999) 227 – 264.
- [24] G. Batchelor, *An introduction to fluid dynamics*, Cambridge Univ. Press, 2000.
- [25] P. J. Davis, *Circulant matrices*, Pure and applied mathematics A Wiley-Interscience publication, Wiley, New York [u.a.], ISBN 0-471-05771-1, 1979.
- [26] D. Violeau, A. Leroy, A. Joly, A. Hérault, Spectral properties of the SPH Laplacian operator, *Computers & Mathematics with Applications* 75 (2018) 3649–3662.
- [27] S. Litvinov, X. Hu, N. Adams, Towards consistence and convergence of conservative SPH approximations, *Journal of Computational Physics* 301 (2015) 394–401.
- [28] M. Antuono, A. Colagrossi, S. Marrone, Numerical diffusive terms in weakly-compressible SPH schemes, *Computer Physics Communications* 183 (12) (2012) 2570–2580.
- [29] F. Maciá, M. Antuono, L. M. González, A. Colagrossi, Theoretical analysis of the no-slip boundary condition enforcement in SPH methods, *Progress of theoretical physics* 125 (6) (2011) 1091–1121.

Appendix A. Expressing perturbation equation as a matrix system

This section illustrates how the perturbation equations can be cast into a matrix system for a simplified case. Let us consider Eq. 15b where only the term proportional to W'' is present:

$$\frac{d^2 \delta x_a}{dt^2} = -2 \frac{\bar{p} \bar{V}}{\bar{\rho}} \sum_b (\delta x_{ab}) W''_{ab} \quad (\text{A.1})$$

Focusing on particle 0 at the left of the domain (see Fig. 1) and considering a sphere of influence containing 5 particles (*i.e.* $M=2$), the equation of motion is explicitly expressed as:

$$\begin{aligned} \frac{\bar{\rho}}{2\bar{p}\bar{V}} \frac{d^2 \delta x_0}{dt^2} = & + \delta x_{N-2} W''(2\Delta x) \\ & + \delta x_{N-1} W''(\Delta x) \\ & - \delta x_0 [W''(2\Delta x) + W''(\Delta x) + W''(-\Delta x) + W''(-2\Delta x)] \\ & + \delta x_1 W''(-\Delta x) \\ & + \delta x_2 W''(-2\Delta x) \end{aligned} \quad (\text{A.2})$$

Gathering all particle perturbations into the vector $\underline{X} = (\delta x_0, \delta x_1, \delta x_2, \dots, \delta x_{n-1})^T$, Eq. A.1 can be expressed as a matrix system:

$$\frac{d^2}{dt^2}(\underline{X}) = 2 \frac{\bar{p} \bar{V}}{\bar{\rho}} \underline{A}'' \underline{X} \quad (\text{A.3})$$

where the matrix \underline{A}'' is given by:

$$\underline{A}'' = \begin{bmatrix} c_0 & W''(-\Delta x) & W''(-2\Delta x) & 0 & \dots & 0 & W''(2\Delta x) & W''(\Delta x) \\ W''(\Delta x) & c_0 & W''(-\Delta x) & W''(-2\Delta x) & 0 & \dots & 0 & W''(2\Delta x) \\ W''(2\Delta x) & W''(\Delta x) & c_0 & W''(-\Delta x) & W''(-2\Delta x) & 0 & \dots & 0 \\ \dots & \dots \\ W''(-2\Delta x) & 0 & \dots & 0 & W''(2\Delta x) & W''(\Delta x) & c_0 & W''(-\Delta x) \\ W''(-\Delta x) & W''(-2\Delta x) & 0 & \dots & 0 & W''(2\Delta x) & W''(\Delta x) & c_0 \end{bmatrix}$$

with:

$$c_0 = -[W''(-2\Delta x) + W''(-\Delta x) + W''(\Delta x) + W''(2\Delta x)] \quad (\text{A.4})$$

\underline{A}'' is a circulant matrix which is entirely defined by one line or one column. For instance, the vector of the first row:

$$C = (c_0, W''(-\Delta x), W''(-2\Delta x), 0, \dots, 0, W''(2\Delta x), W''(\Delta x)) \quad (\text{A.5})$$

contains all the matrix coefficients. Circulant matrices enjoy the property to be diagonalizable in the same basis, composed of the n -th root of unity [25]. Therefore, \underline{A}'' can be written as:

$$\underline{A}'' = \underline{P}^{-1} \underline{\Delta}'' \underline{P} \quad (\text{A.6})$$

with \underline{P} is the change-of-basis matrix of general term:

$$p_{ij} = \frac{1}{\sqrt{N}} \exp\left(\hat{i} \frac{2\pi}{N} ij\right) \quad (\text{A.7})$$

where \hat{i} is the imaginary number. The diagonal matrix $\underline{\Delta}'' = \text{diag}(\lambda''_0, \lambda''_1, \lambda''_2, \dots, \lambda''_{N-1})$ in Eq. A.6 is expressed in the general case by:

$$\lambda''_j = \sum_{k=0}^{N-1} c''_k \exp\left(\hat{i} \frac{2\pi}{N} kj\right) \quad (\text{A.8})$$

Appendix B. Validation of temporal solutions

This section provides a validation of the derivation of the perturbations equation for each of the four methods. Therefore the temporal solutions provided for each method are compared to the results of a simple numerical scheme. Two types of perturbations are investigated. First, an inviscid flow ($\nu=\alpha=0$), where only the particle at the center of the domain is perturbed. Second, a viscous flow ($\nu=0.1$, equivalently $\alpha=0.2$ for δ -SPH), where all particles are following an initial sinusoidal perturbation. In this case, two different modes are investigated.

In both cases, the initial perturbed value as well as the intensity of the perturbation was varied depending on the method (Table B.1). This was done in order to illustrate different initial configurations, but every SPH method was extensively tested with all types of initial perturbations. The domain is a periodic line composed of 63 particles ($N=63$) and each particle has 6 neighbors ($M=3$). The time integration of the numerical scheme is a first-order sequential explicit scheme [15], and the time step Δt is selected according to:

$$\Delta t = C_{\Delta t} \min(\Delta t_{\nu}, \Delta t_{CFL}) \quad \text{where} \quad \Delta t_{\nu} = \frac{1}{8} \frac{\Delta x^2}{\nu} \quad \text{and} \quad \Delta t_{CFL} = \frac{1}{4} \frac{\Delta x}{c + u_{max}} \quad (\text{B.1})$$

The constant $C_{\Delta t}$ was introduced because the different SPH methods show different accuracies depending on the time integration. Its values are recalled in Table B.1. Please note that these differences of accuracy depicts the sensitivity of each method to the numerical integration scheme used to produce the reference temporal solution. The analytical temporal solution provided by our derivation do not require any time integration. According to the analysis by Violeau and Leroy [15] on the stability of the integration scheme, the combination of the sequential scheme with the constants in Eqs. B.1 and the constants in Table B.1 ensures that the scheme is stable. Other parameters are $p_{bg}=1$, $c=1$ and $\gamma=7$.

Specific parameters for δ -SPH are $\alpha = 2\nu$, $\xi = \alpha/4$, $\chi = \xi$ and $\Gamma = 0.151$. The latter was estimated as proposed by Antuono et al. [17] by taking into account the background pressure in the equation of state. For TV-SPH, both physical and transport velocities are set to zero unless it is mentioned.

Table B.1: Perturbed quantities and integration time constant used in test cases 1 and 2.

Parameter	sum-SPH	div-SPH	δ -SPH	TV-SPH
Perturbed value	u	x	ρ	x
δ_0	$0.1 c$	$0.1 \Delta x$	$0.1 \bar{\rho}$	$0.1 \Delta x$
$C_{\Delta t}$	1	0.5	0.1	1

For sum-SPH and div-SPH, the analytical solution is directly compared to the results of the simulation. Therefore, Eqs. 44, 47 and 48 are compared to the numerical solution of the system 6 for sum-SPH, and Eqs. 59, 60 and 61 are compared to the numerical solution of the system 53 for div-SPH. Concerning δ -SPH and TV-SPH, no analytical solutions were derived. Therefore, the transfer functions in the Laplace domain were decomposed into simple complex rational functions using partial fraction decomposition for each temporal mode i :

$$P_i(p) = \frac{z_1}{p - z_2} + \frac{z_3}{p - z_4} + \frac{z_5}{p - z_6} \quad (\text{B.2})$$

where z_j are complex numbers. Then, each simple rational function is transformed into a temporal function using the identity:

$$\mathcal{L}^{-1} \left[\frac{\alpha}{p - \beta} \right] = \alpha \exp(\beta t) \quad \text{for} \quad p > \text{Re}(\beta) \quad \text{and} \quad (\alpha, \beta) \in \mathbb{C}^2 \quad (\text{B.3})$$

The temporal functions are then transformed into the geometrical space using the general change-of-basis formula for circulant matrix:

$$F_{ij}(t) = \frac{1}{N} \left[\sum_{k=0}^{N-1} f_k(t) \exp \left(i \frac{2\pi}{N} k(i - j) \right) \right] \quad (\text{B.4})$$

This last operation is equivalent to expressing the matrices \underline{A}' , \underline{A}'' and \underline{A}''' into their original basis. One can observe that Eqs. 48 and 61 are particular cases of Eq. B.4. The functions $F_{ij}(t)$ are finally compared to the numerical solutions of the original system, Eqs. 62 for δ -SPH and Eqs. 69 for TV-SPH.

Appendix B.1. Case 1: inviscid flow with a single perturbed particle

In this subsection, the position of the initially perturbed particle (δx_{31}) and the particle which is located furthest away (δx_0) are shown. Figure B.26 (left) shows the comparison with sum-SPH, where the initial velocity was perturbed by $0.1c$. The comparison with div-SPH is shown in Fig. B.26 (right). It is observed that the perturbed particle (δx_{31}) does not oscillate around the equilibrium position, but around a position shifted by ≈ -0.5 , as predicted by the constant term in Eq. 59a. The temporal solution shows a superposition of several modes, which are retrieved by our derivations. For both methods, the agreement is excellent, even for a large perturbation of $0.1c$ and $0.1\Delta x$. The time delay of the information propagation, visible on particle 0, is well taken into account.

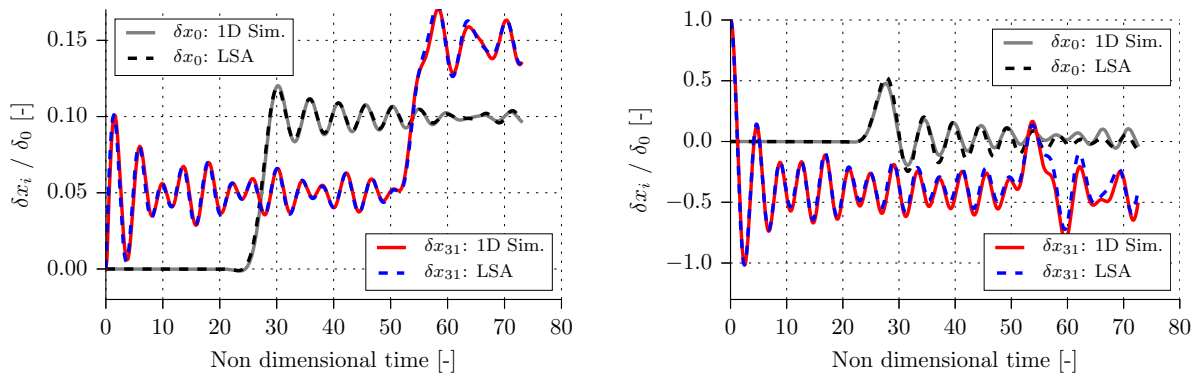


Figure B.26: Comparison of LSA solution with a 1D SPH simulation. Left: sum-SPH. Right: div-SPH.

The comparison with δ -SPH and TV-SPH are shown in Fig. B.27. For δ -SPH, the perturbed position δx_{31} of particle 31 was constant over the time so the position δx_{30} of the next particle is presented. The slight discrepancy for δx_{30} is attributed to the sensitivity of the δ -SPH method to the time integration. For instance, an initial perturbation of $0.01 \bar{p}$ gives an excellent agreement. This sensitivity to the integration scheme highlights the need for a subsequent study on the influence of the integration scheme on this particular method, as proposed by Violeau and Leroy [15]. In the comparison with TV-SPH (Fig. B.27 right), δx_0 was artificially shifted by $+0.5$ for the sake of clarity. It also shows a good agreement between LSA and SPH simulation.

Appendix B.2. Case 2: viscous flow with a spatial sinusoidal perturbation

For this test case, all particles are spatially perturbed according to a cosine function. Two different modes are investigated. With a wavelength of almost two time the diameter of the sphere of influence, mode 5 represents *resolved* oscillations. Mode 31 is investigated as it represents high frequency spatial oscillations which are prone to instability. Since in mode 31, every consecutive particle is shifted in the opposite 'direction', the perturbation amplitude is set to $\delta_0/2$ in this case compared to δ_0 for mode 5.

The comparison between LSA and SPH simulation is presented in Figs. B.28 and B.29 where the agreement is excellent for all methods. For TV-SPH (Fig. B.29 right), the mode 31 is not damped, as it was highlighted by the dispersion curve discussion in Section 6.

Finally, in Fig. B.30 mode 5 and 31 are shown for TV-SPH with $(\bar{u}, \bar{w}) = (0.05, 0.1)$ during a long time simulation. The instabilities exhibited in Fig. 21 are visible but with a larger growth rate in the 1D simulation compared to LSA. This deviation of growth rate is probably due to the first-order time integration scheme of the numerical method.

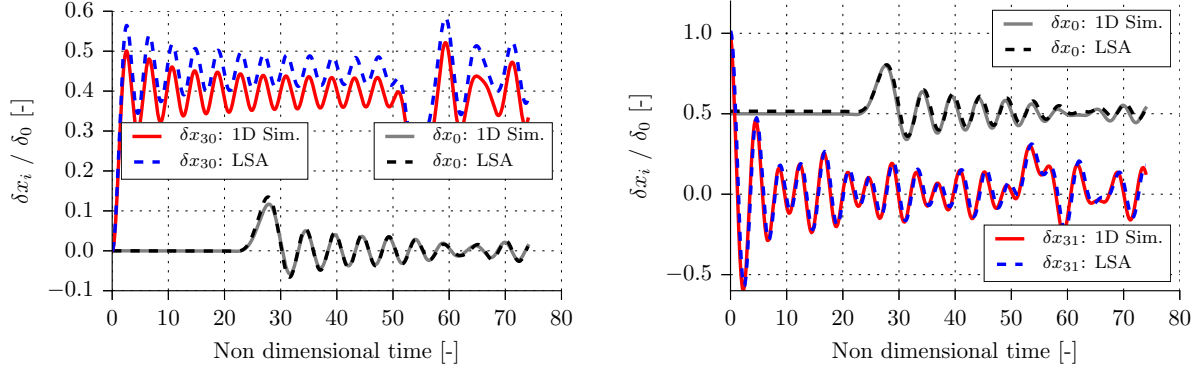


Figure B.27: Comparison of LSA solution with a 1D SPH simulation. Left: δ -SPH. Right: TV-SPH, $(\bar{u}, \bar{w})=(0,0)$, δx_0 was shifted of $+0.5$ for the sake of clarity.

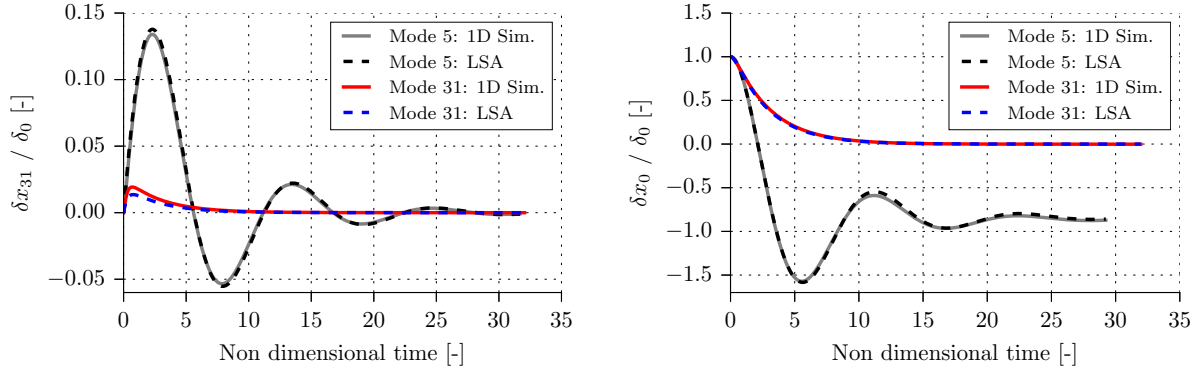


Figure B.28: Left: sum-SPH. Right: div-SPH

As a conclusion of this validation part, the temporal solutions provided by our derivations perfectly match the solutions provided by the numerical resolution of the original systems of equations. In the case of a single perturbed particle, which corresponds to a continuous spectrum of excitations, the temporal solutions shows a superposition of all modes. This means that all modes predicted by our derivation are well retrieved in the numerical simulation. In addition, the caveats highlighted by the dispersion curves are also well illustrated by the numerical simulations. Indeed, the div-SPH method fails to damp a perturbation of position (Figs. B.26 right and B.28 right), while the TV-SPH method do not damp the mode of higher frequency (Figs. B.29 right).

Appendix C. Validation of the instability at large background pressure

In this subsection the instability at large background pressure presented in Section 2.6.2 is verified. The SPH method is sum-SPH, and the other numerical parameters are the same as in the previous subsection. The setup consists of a line of 500 particles perturbed at lower modes ($1 \rightarrow 9$) where the instability arises. Two additional modes are tested, mode 50 and 125. The Wendland kernel is used with a M parameter of 3. The particles are perturbed by a sinusoidal velocity whose amplitude is equal to 1% of the sound speed, and the simulation is run for ten thousand time step. For each investigated mode, the background pressure is set 50, 70, 90, 100, 110, 130 and 150% of the predicted critical pressure. For modes 9, 50 and 125, the critical

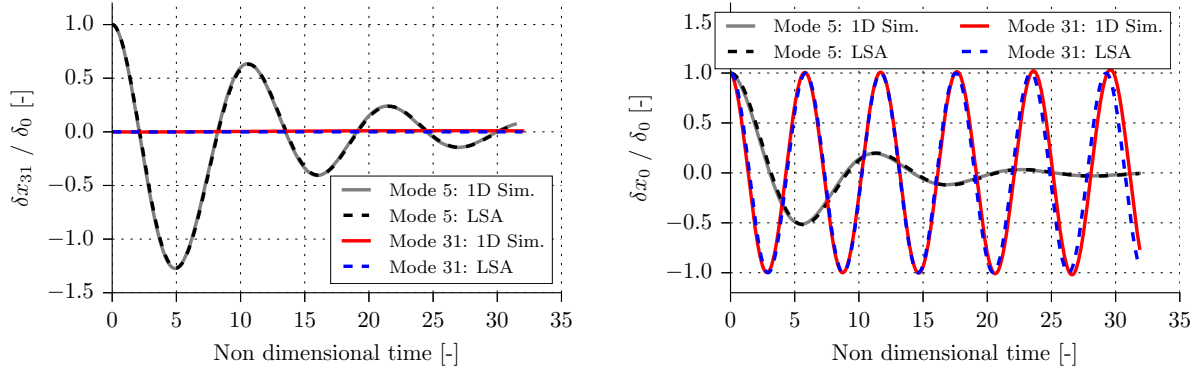


Figure B.29: Left: δ -SPH. Right: TV-SPH

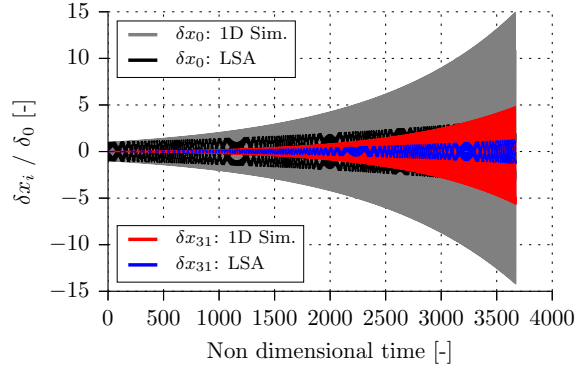


Figure B.30: Slow divergence of TV-SPH in case of constant velocities: $(\bar{u}, \bar{w}) = (0.05, 0.1)$

pressure was set after preliminary tests. The stability of the system is monitored with the value of the time step. Due to the CFL condition, the time step sharply decreases in case of a larger velocity triggered by an instability.

The results are shown in Fig. C.31. The agreement is good. Up to mode 5, the instability arises for p_i between 70 and 90% of the theoretical value, and between 90 and 110% for modes 6, 7, and 8. It is found that the numerical simulations are unstable for larger modes whereas the theory does not predict any instability. Its possible origin could be due to the deterioration of the spatial perturbation. Due to many oscillations, the accuracy of the particle positions would decrease because of the truncation error of float numbers. This would lead to a spatial perturbation composed of different modes, including the unstable ones.

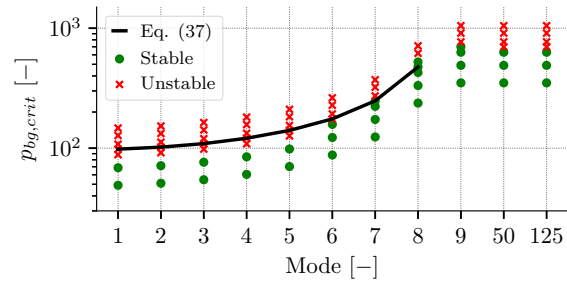


Figure C.31: Comparison between the analytical value of Eq. 37 and the results of the numerical simulation.